Pharmacological Research 221 (2025) 107973

Contents lists available at ScienceDirect

Pharmacological Research

journal homepage: www.elsevier.com/locate/yphrs

Imaging of mitochondrial matrix pH dynamics reveals a functional interaction between the ADP/ATP carrier and ATP synthase to regulate H^+ distribution

Bernard Ribalet [a,*], Scott John [b], Madeleine G. Milner [a], Leia Salongo [a], Ambre M. Bertholet [a,*]

[a] Department of Physiology, David Geffen School of Medicine at UCLA, Los Angeles, CA, United States
[b] Department of Medicine (Division of Cardiology), David Geffen School of Medicine at UCLA, Los Angeles, CA, United States

ARTICLE INFO

Keywords:
Mitochondria
Proton transport
PH sensor
ADP/ATP carrier
ATP synthase
Electron transport chain
Uncoupling protein
BAM15
FCCP

ABSTRACT

In mitochondria, the energy derived from the proton gradient across the mitochondrial inner membrane (IMM) is converted into ATP and heat. For these conversions to occur, H^+ is pumped out of the matrix via the electron transport chain (ETC) and then re-enters either via the ATP synthase to produce ATP or via the ADP/ATP carrier (AAC) to release heat. Due to its dual functions of ADP/ATP exchange and H^+ transport, AAC may be considered a major regulator of the energy distribution of mitochondria between ATP synthesis and thermogenesis. Using real-time imaging of pH with a fluorescent pH probe targeted to the mitochondrial matrix, we investigated in a myoblast cell model how H^+ fluxes across the IMM are regulated by AAC and the ATP synthase. Our data show that activation of AAC-dependent H^+ transport by the mitochondrial uncoupler BAM15 causes an acidification of the matrix followed by a re-alkalization phase due to the reversed activity of the ATP synthase. Similar re-alkalization and reversal of ATP synthase activity were observed after acidification caused by inhibition of the electron transport chain. Lastly, the discovery that strong protonophoric activity independent of AAC suppresses the re-alkalization phase and consequently the reverse action of the ATP synthase, suggests the need for strict control of the H^+ flux through the IMM by AAC. Thus, real-time imaging of matrix pH reveals a functional interaction between AAC and the ATP synthase for the control of H^+ fluxes across the IMM.

1. Introduction

Mitochondria transform the energy contained in consumed nutrients into the two forms of chemical energy within the cell, ATP and heat, and a dynamic balance between these forms of energies is vital for mitochondria to adapt to the metabolic needs of cells. Nutrients are first converted into high energy electron donors, which fuel the electron transport chain (ETC) to pump hydrogen ions (H^+) out of the mitochondrial matrix through complexes I, III, and IV, which create a H^+ gradient across the IMM that is used as a source of energy [17,25,46]. H^+ then flow back down this gradient and into the matrix via the ATP synthase to produce ATP. The H^+ gradient is also used by a process that bypasses the ATP synthase and involves uncoupling proteins (UCPs), specific H^+ transporters in the IMM, and the resulting energy is simply released as heat [25,10]. This process is referred to as mitochondrial thermogenesis, and its function is essential for maintaining body temperature and regulating energy expenditure [21,10]. Increasing mitochondrial thermogenesis reduces fat depots and provides an effective way to combat the metabolic syndrome that can be achieved using small molecules such as 2,4-dinitrophenol (DNP), carbonyl cyanide-p-trifluoromethoxyphenylhydrazone (FCCP), and N5,N6-bis (2-fluorophenyl)-[1,2,5]oxadiazolo[3,4-*b*]pyrazine-5,6-diamine (BAM15) [19,4,32,47,48,56]. These compounds have been classed as protonophores, meaning they transport H^+ across all biological membranes without the involvement of any membrane protein [56]. Studies conducted in rodent and nonhuman primate models of metabolic syndrome have shown that uncouplers reduce the severity of hepatic steatosis and of insulin resistance in type II diabetes [47,48]. These findings make uncouplers one of the most effective anti-obesity and anti-diabetes drug candidates described to date [47,48]. Unfortunately, due to their significant side effects, there remains a need for safer and yet powerful compounds that can induce mitochondrial thermogenesis without affecting other cellular functions.

Until recently, the identity of the UCP responsible for mitochondrial

* Corresponding authors.
E-mail addresses: bribalet@mednet.ucla.edu (B. Ribalet), abertholet@mednet.ucla.edu (A.M. Bertholet).

https://doi.org/10.1016/j.phrs.2025.107973
Received 23 July 2025; Received in revised form 12 September 2025; Accepted 24 September 2025
Available online 25 September 2025

thermogenesis had not been clearly established [10]. Using the patch-clamp technique applied to mitochondria, we discovered that the ADP/ATP carrier (AAC), the protein responsible for the ADP/ATP exchange essential for ATP production, is the main UCP in non-adipose tissues such as heart, skeletal muscle, liver, and kidney [6,7]. The AAC mechanism of H^+ transport is close to that of Uncoupling Protein 1 (UCP1), the main UCP in beige and brown adipocytes [27,7,8]. Interestingly, UCP2 and UCP3, which are the closest homologs to UCP1 and considered to be the UCPs of non-adipose tissues, were not responsible for the H^+ current induced across the IMM of the different tissues tested in our electrophysiological recordings [7,10]. Other studies have shown that UCP2 and UCP3 proteins can transport C3-C4 metabolites, thereby challenging the idea that UCP2 and UCP3 proteins can transport H^+ into mitochondria and impact mitochondrial thermogenesis in the same way as AAC [13,14,23,35,41,61]. We also directly measured the H^+ transport induced by the common uncouplers DNP, FCCP, SF6847, and the mitochondrial specific BAM15 and helped redefine their mode of action [11,32]. Surprisingly, although these chemical uncouplers are considered protonophores, their major effect in heart mitochondria was found to be via the induction of H^+ current through AAC [11]. Thus, due to its dual functions controlling ATP production and heat, we propose AAC as the crucial determinant of energy expenditure, metabolic efficiency, and body temperature. These findings provided the first molecular basis for targeting AAC to treat obesity and diabetes.

From the perspective of the mitochondrial H^+ gradient, the distribution of mitochondrial energy between ATP and heat can be studied through the flow of H^+, which must be distributed between AAC and the ATP synthase [17,46,10]. We therefore propose that AAC plays an important role in the energy distribution between heat and ATP by regulating H^+ pools across the IMM.

In the present study, we investigated how AAC-dependent H^+ transport controls H^+ pools across the IMM using real-time pH imaging in C2C12 myoblast cells and pharmacological agents. Since the H^+ gradient across IMM can fluctuate rapidly as a function of time, changes in H^+ flux require acute pharmacological induction as well as recording techniques capable of monitoring fast events. These techniques, which include electrophysiological measurements in isolated mitochondria and pH imaging in the matrix of living cells, are difficult to perform *in vivo*. One of the innovations in our present study is the use of the chemical uncoupler BAM15 as the primary tool to induce AAC-dependent H^+ transport in heart mitochondria and C2C12 cells. Already characterized for specifically inducing H^+ flux into mitochondria by the team that discovered it, our previous work was the first to establish the molecular target of BAM15, which, instead of being a pure protonophore, exerts approximately 85 % of its action via AAC in cardiac mitochondria [11,32]. We also previously tested FCCP and showed that 50 % of its effect is mediated by AAC, while the remaining 50 % might be the result of high protonophoric activity [11]. Based on our electrophysiological data obtained from cardiac mitochondria, we chose for the present study low and high concentrations of BAM15 and FCCP, which induced measurable H^+ currents with a 10-fold difference in amplitude. Although the lower concentration may be more physiologically relevant, we wanted to investigate how large protonophoric currents affect the regulation of the H^+ pools across the IMM independently of AAC. Our real-time pH measurements using the pH probe Super-Ecliptic pHluorin (SE-pHluorin) [39] targeted to the mitochondrial matrix of C2C12 cells show that increasing H^+ influx via AAC using BAM15 induces matrix acidification followed by a re-alkalization phase. The latter involves the reversed activity of the ATP synthase, regardless of the concentration of BAM15. Only low concentrations of FCCP could induce the ATP synthase to function in the reverse mode. The reversal of the ATP synthase activity is likely to occur when the AAC-dependent H^+ current is not masked by elevated protonophoric current induced by high concentrations of FCCP. Inhibition of ETC by agents used in other cellular studies at concentrations known to induce the reverse action of ATP synthase also triggers a phase of mitochondrial matrix acidification, followed by a phase of ATP synthase-dependent re-alkalization. These observations validate our pH measurements as a useful tool for studying the distribution of H^+ fluxes across the IMM.

Overall, our results demonstrate that AAC-dependent H^+ transport tightly regulates the reversed activity of the ATP synthase in C2C12 cells to control the H^+ gradient across the IMM.

2. Materials and methods

2.1. Animals

Mice were maintained on a standard rodent chow diet under 12-h light and dark cycles. All animal experiments were performed with male mice (aged 2–5 months) according to procedures approved by the UCLA Institutional Animal Care and Use Committee under animal protocol ARC-2020–169 supervised by AMB. UCLA's Animal Welfare Assurance number with the Department of Health and Human Services Office of Laboratory Animal Welfare is D16–00124 (A3196–01). UCLA's animal care and use program is fully accredited by AAALAC, International. C57BL/6 J mice were purchased from the Jackson Laboratory. Sample size was based on the results of pilot experiments to ensure that statistical significance could be reached. A limitation to the generalizability of the study is that it did not consider gender/sex issues.

2.2. Isolation of mitochondria and mitoplasts from heart tissue

Mice were euthanized by CO_2 asphyxiation followed by cervical dislocation. For the preparation of mitoplasts, mouse heart tissue was isolated, rinsed, and homogenized in ice-cold medium containing 250 mM sucrose, 10 mM HEPES, 1 mM EGTA, and 0.1 % bovine serum albumin (BSA) (pH adjusted to 7.2 with Trizma base) using a glass grinder with six slow strokes of a Teflon pestle rotating at 275 rotations per minute. The homogenate was centrifuged at 700 *g* for 5–10 min to pellet nuclei and unbroken cells. The first nuclear pellet was resuspended in the same solution and homogenized again to increase the yield of mitochondria. Mitochondria were collected by centrifugation of the supernatant at 8500 *g* for 10 min.

Mitoplasts were produced from mitochondria using a French press. In brief, mitochondria were suspended in a solution containing 140 mM sucrose, 440 mM d-mannitol, 5 mM HEPES, and 1 mM EGTA (pH adjusted to 7.2 with Trizma base) and then subjected to a French press at 1200–2000 psi to rupture the outer membrane. Mitoplasts were pelleted at 10,500 *g* for 15 min and resuspended for storage in 500 µl of solution containing 750 mM KCl, 100 mM HEPES, and 1 mM EGTA (pH adjusted to 7.2 with Trizma base). Mitochondria and mitoplasts were prepared at 0–4 °C and stored on ice for up to 5 h. Immediately before the electrophysiological experiments, 15–50 µl of the mitoplast suspension was added to 500 µl solution containing 150 mM KCl, 10 mM HEPES, and 1 mM EGTA (pH adjusted to 7.0 with Trizma base) and plated on 5-mm coverslips pretreated with 0.1 % gelatin to reduce mitoplast adhesion.

2.3. Mitochondrial patch-clamp recordings

Patch-clamp recording was performed from isolated mitoplasts. The mitoplasts used for patch-clamp experiments were 2–4 µm in diameter and typically had membrane capacitances of 0.3–1.2 pF. Gigaohm seals were formed in the bath solution containing 150 mM KCl, 10 mM HEPES, and 1 mM EGTA (pH 7 adjusted with Trizma base). Voltage steps of 250–500 mV and 1–50 ms were applied to break-in into the mitoplast and obtain the whole-mitoplast configuration, as monitored by the appearance of capacitance transients. Mitoplasts were stimulated every 5 s. Currents were normalized per membrane capacitance to obtain current densities (pA/pF).

All indicated voltages represent the voltages on the matrix side of the IMM (pipette solution) as compared to the cytosolic side (bath solution, defined to be 0 mV). Normally, currents were induced by a voltage ramp

from −160 mV to + 100 mV to cover all physiological voltages across the IMM. Currents flowing into mitochondria are shown as negative, while those flowing out are positive. Membrane capacitance transients observed upon application of voltage steps were removed from current traces.

Both the bath and pipette solutions were formulated to record H^+ currents and contained only salts that dissociate into large anions and cations that are normally impermeant through ion channels or transporters. In the majority of experiments, we used a low pH gradient across the IMM (pH 7.5 and 7.0 on the matrix and cytosolic sides, respectively) to approximate physiological conditions. However, other pH gradients were also used as indicated.

Pipettes were filled with 130 mM tetramethylammonium hydroxide (TMA), 1.5 mM EGTA, 2 mM Tris chloride, and 100 mM HEPES (or MES). pH was adjusted to 7.5 with d-gluconic acid, and tonicity was adjusted to ~360 mmol/kg with sucrose. Typically, pipettes had resistances of 25–35 MΩ, and the access resistance was 40–75 MΩ.

The whole-mitoplast H^+ current was recorded in the bath solution containing 100 mM HEPES and 1 mM EGTA (pH adjusted to 7.0 with Trizma base, and tonicity adjusted to ~300 mmol/kg with sucrose).

All experiments were performed under continuous perfusion of the bath solution. All electrophysiological data presented were acquired at 10 kHz and filtered at 1 kHz.

2.4. Solutions and experimental techniques for imaging of matrix pH

The bath solution for cell imaging contained 140 mM NaCl, 5 mM KCl, 1.1 mM $MgCl_2$, 2.5 mM $CaCl_2$, 10 mM HEPES (pH adjusted to 7.2 with NaOH), and 10 mM glucose. *N*-methyl-*d*-glucamine was added to maintain the solutions' osmolarity when glucose was removed. Solutions were perfused directly over the cells using a gravity-fed eight-way perfusion device (Warner Instruments, Hamden, CT, USA) with electrically controlled solenoids (The Lee Company, Westbrook, CT, USA). Input and output of solution volumes to the recording chamber (glass bottomed Petri dish) were equilibrated to maintain constant flow rates and pressures within the recording chamber. Currents were recorded in response to treatment with the following individual agents: oligomycin (Sigma Aldrich, 495455), BAM15 (MedChemExpress, HY-110284), rotenone (Millipore Sigma, R8875), FCCP (Enzo Life Sciences, BML-CM120–0010), antimycin A (Sigma Aldrich, A8674), and sodium cyanide (NaCN, Sigma, S-3296).

2.5. AAC1 and AAC2 DKO and AAC1 overexpression in C2C12 cells. Molecular biology and cell culture

The C2C12 cell line was originally purchased from ATCC (https://www.atcc.org/) and cultured in complete Dulbecco's modified Eagle's medium (DMEM; with 25 mM glucose, 10 % fetal bovine serum [FBS], penicillin and streptomycin antibiotics). The C2C12 cell line was authenticated by ATCC. AAC1/AAC2 DKO C2C12 cells were generated by Alstem LLC (http://www.alstembio.com/) using the CRISPR–Cas9 system and characterized in our previous studies [11,7]. All cell lines tested negative for mycoplasma contamination. For AAC1 reintroduction, we used lentiviruses produced by Vector Builder to transduce DKO C2C12 cells. Green fluorescent protein (GFP) was used as a selection marker.

2.6. SE-pHLuorin fluorescent sensor

Complementary DNA (cDNA) for Super-Ecliptic pHluorin (SE-pHluorin) was purchased from Addgene [39]. It was subcloned into the pcDNA3.1 amp mammalian expression vector (Invitrogen) (Fig. 2A) and used to transfect C2C12 cells with Lipofectamine 2000 (Invitrogen). Fluorescence measurements were performed after 36 h. The sensor is highly sensitive to changes in pH in the physiological range [12,51] and exhibits a nearly linear response between pH 7.2 and 7.8. Importantly, our calibration curve shown in Fig. 2D indicates that the changes in pH that we recorded in our experiments fall within the probe dynamic range (Supplementary Figure 2). Based on our calibration curve (Fig. 2D), we may conclude, for example, that BAM15-induced mitochondrial acidification lowers the matrix pH from 7.8 to 7.0.

2.7. Fluorescence imaging

For imaging the SE-pHluorin expressed in the mitochondrial matrix, we used a dual-emission, single excitation method similar to that described by Rossano et al. Rossano et al., [51]. They used a 406/20 nm exciter filter, a 500-nm dichroic mirror mounted in the emission beam-splitter, and two emission filters centered at 485/35 nm and 536/30 nm, and their set up is very similar to the fluorescence resonance energy transfer (FRET) set up that we previously used for cyan fluorescent protein (CFP)/yellow fluorescence protein (YFP) FRET measurements [30,31]. In the present study, the excitation wavelength was slightly shifted, but the measurements showed excellent signal-to-noise ratios.

Images (16-bit) were acquired using a Nikon Eclipse TE300 microscope fitted with a × 60 (N.A. 1.4) oil immersion lens (Nikon) and equipped with a CFP/YFP FRET filter set up. The excitation used a CFP bandpass excitation filter, 440/20b, together with a longpass dichroic filter (Chroma Technology Corp, Rockingham, VT, USA). A light-emitting diode (LED, Lumileds, San Jose, CA, USA) was used as the light source emitting at 455 ± 20 nm (royal blue). The LED and camera exposure were controlled by MetaFluor Imaging 6.1 software (Molecular Devices, Sunnyvale, CA, USA). Ratiometric fluorescence measurements were performed by simultaneously monitoring emissions using a Dual View image splitter (Optical Insights, Tucson, AZ, USA) equipped with a 505-nm long-pass dichroic filter and two emission filters centered at 480/30 nm and 535/40 nm. This set up provided two separate images simultaneously, corresponding to the emissions of the sample at 480 and 535 nm when excited at 440 nm (royal blue LED). The ratio between the two emission wavelengths was measured online in real time using MetaFlour Imaging software. For analysis, background light intensity was subtracted from the individual emission. Superposition of the 480 nm and 535 nm images was carried out using the imaging software. Images were captured with a Cascade 512B digital camera (Photometrics, Tucson, AZ, USA). Exposure times were optimized in each case but varied between 100–500 ms and were recorded at a constant rate for each cell between 0.2–0.33 Hz. For experiments lasting more than 30 min, a slow drift in the ratio baseline was sometime observed. In such cases, the drift was corrected using linear curve fitting; in others, the drift was corrected using exponential curve fitting. At the end of each experiment, the preparation was exposed to a pulse of 20 mM NH_4Cl to confirm the sensitivity of the pH probe in situ. The response to NH_4Cl was used to normalize the change in pH measured under the different experimental conditions.

2.8. Calibration of the SE-pHluorin sensor in permeabilized cells

To calibrate the pH sensor, C2C12 cells were first transfected with the SE-pHluorin sensor targeted to the mitochondrial matrix. As shown in Supplementary Figure 2A, the cells were first exposed to a solution with 100 μM β-escin at pH 7.0 (Escin, Sigma, E1378). Cell permeabilization was detected once the fluorescence ratio dropped within 15–30 s. The perfusion was then switched to a solution without β-escin at pH 7.8. Thereafter, solutions with pH between 6.8–8.0 were perfused. Notably, the values at pH < 6.5 are highly constant due to quenching of the sensor at these acidic pHs. Even though the light signal intensity decreases over time as the sensor leaks out of the mitochondria and out of the cell, the initial value measured for a solution with a pH of 7.8 is closer to the value measured for the mitochondrial matrix before membrane permeabilization. This observation suggests that the pH of the matrix is close to 7.8, in accordance with other reports [52,1]. The

slope and pH0.5 (7.49) of the calibration curve are very similar or identical to in vivo measurements calibration reported by others [12, 51]. Finally, we can predict, based on this calibration curve and the values of the ratios reported in this study for various experimental conditions, that the acidification of the matrix pH evoked by "commonly used" concentrations of uncouplers are within the dynamic range of the SE-pHluorin sensor (Fig. 1D).

2.9. Extracellular flux analysis of C2C12 cells

All oxygen consumption measurements were conducted using an Agilent Seahorse XF96 or XFe96 Analyzer. Cells were seeded at 20,000 cells/well in a 96-well microplate, 8 h before the start of the assay. Experiments were conducted at 37°C and pH 7.4. Only the inner 60 wells were used, and the outer rim was filled with 200 µl phosphate-buffered saline (PBS) throughout the incubation to minimize variance in temperature and evaporative effects across the plate. Cellular respiration

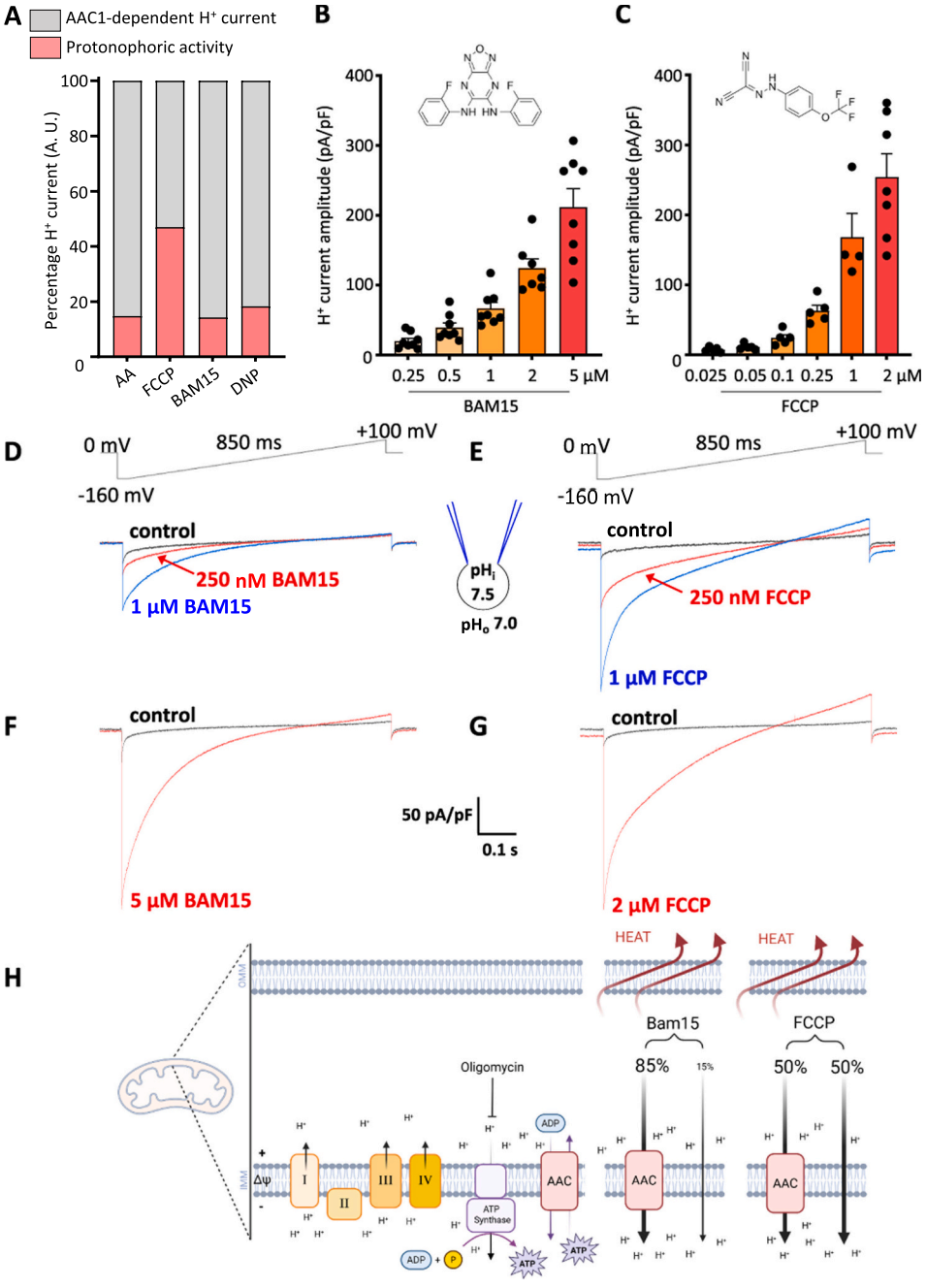

Fig. 1. BAM15 activates H^+ current mainly through AAC. A. Graph representing ratio of AAC1-dependent H^+ current (grey) and the non-specific protonophoric activity (light red) from previous characterization induced by long chain fatty acid arachidonic acid (AA), FCCP, BAM15 and DNP [11,7]. B. H^+ current densities at −160 mV in heart mitoplasts with different BAM15 concentrations. Data are mean ± s.e.m. n = 7–8 mitoplasts for all conditions. C. H^+ current densities at −160 mV in heart mitoplasts with different FCCP concentrations. Data are mean ± s.e.m. n = 4–7 mitoplasts for all conditions. D to G. Representative H^+ current induced by 250 nM BAM15 (D, red trace), 1 µM BAM15 (D, blue trace), and 5 µM BAM15 (**F**, red trace) in heart mitoplasts. Representative H^+ current induced by 250 nM FCCP (**E**, red), 1 µM FCCP (**E**, blue), and 2 µM FCCP (**G**, red) in heart mitoplasts. The voltage ramp protocol is shown above the traces. **H.** Scheme representing the mode of action of BAM15, which is mainly to induce H^+ transport through AAC, and the mode of action of FCCP, which partly induces H^+ transport through AAC and has high protonophoric activity.

measurements were conducted in Seahorse XF DMEM medium pH 7.4 supplemented with 10 mM glucose, 2 mM glutamine, and 2 mM Na^+-pyruvate. Respiration was measured before and after injection of 1 μM oligomycin (Sigma Aldrich 495455, 3 μM BAM15 (MedChemExpress, HY-110284), which was injected twice, and 1 μM rotenone (Millipore Sigma, R8875) with 2 μM antimycin A (Sigma Aldrich, A8674). Cell counts were performed by incubating cells in a 1:500 dilution of Hoescht 33342 solution for 10 min and measured using an Operetta High-Content Imaging System (Perkin Elmer).

2.10. Immunoblot analysis

For western blot analysis, cells were lysed in radio-immunoprecipitation assay (RIPA) buffer (1 % Igepal, 0.1 % sodium dodecyl sulfate, 0.5 % sodium deoxycholate, 150 mM NaCl, 1 mM EDTA, 50 mM Tris-HCl, pH 7.4) and a cocktail of protease inhibitors. Lysates were resolved by sodium dodecyl sulfate (SDS)–polyacrylamide gel electrophoresis (PAGE), transferred to a polyvinylidene difluoride (PVDF) membrane (Millipore), and probed with anti-Na^+/K^+-ATPase (Abcam, ab76020, GR3237646–13, 1/10,000), anti-TOMM20 (Sigma Prestige, HPA011562, 1/500), and anti-AAC1 (Sigma Aldrich, SAB2108761, 1/100). In the experiment presented in Supplementary Figure 6, we used an antibody recognizing AAC1 and AAC2 isoforms to compare AAC1 protein levels upon reintroduction into DKO C2C12 cells with the total amount of AAC protein in WT C2C12 cells (Abcam, ab110322, 1:1000).

2.11. Curve fitting and statistical analysis

Most changes in fluorescence ratio due to various experimental perturbations were fitted with a single exponential, combination of two exponentials, or a combination of exponential and sigmoid functions (Fig. 1). Data fitting using two exponential functions and a sigmoid function was used with only 10 cells where the initial acidification and re-alkalization phases were rapid and could be clearly distinguished from the slow acidification phase (see Supplementary Figure 3). Even in these cases, the fit involved 8 variable parameters, and strict constraints had to be used to achieve a satisfactory convergence. In theory, all data should be fitted using two exponential and sigmoid functions, but this would require setting arbitrary limits on the parameters, which would not be justified given the good fit of the data using a single exponential and sigmoid function. However, this does not mean that the data do not include two-time constants for acidification, as these two phases are most likely always present, but their values are too close to be separated using exponential fits. It should be noted that the fit obtained for the 10 cells using two exponentials is the most informative approach for these particular recordings.

The fitted amplitude of the emitted signals was then normalized and expressed as a percentage of the control measured with addition of 10 mM NH_4Cl. For experiments involving AAC and ATPase modulators or overexpression of AAC1, we used the same batch of cells (same passage) for the test and control experiments. Histograms with bin size of 10 % were prepared to display the amplitude of the different phases under the various experimental conditions. For the electrophysiology, cell respiration, and mitochondrial membrane potential measurement data, the data are presented as mean ± standard error of the mean (s.e.m.) as specified in the figure legends. Statistical analysis was performed using software GraphPad Prism 10. Statistical significance values were determined as indicated in the figure legends.

3. Results

3.1. BAM15 as a pharmacological tool to induce AAC-dependent H^+ current across the IMM

To investigate how AAC can control the distribution of energy between heat and ATP via the regulation of H^+ pools across the IMM, we used pharmacological tools to induce AAC-dependent H^+ transport. Our previous work using the patch-clamp technique demonstrated that approximately 85 % of the H^+ current induced by BAM15 flows through AAC, compared to 50 % of that induced by FCCP, likely due to a higher protonophoric property (summarized in Fig. 1A, cartoon Fig. 1H) [11]. We therefore used BAM15 as an inducer of AAC-dependent H^+ current and given that only 50 % of FCCP's action is mediated by AAC, we used FCCP to study the effect of a protonophoric activity that also modifies H^+ flux through the IMM independently of a protein.

We first used the mitochondrial patch-clamp technique to identify the concentrations of BAM15 and FCCP that induce similar H^+ current amplitudes across the IMM to compare the effect of the AAC-dependent H^+ current with protonophoric activity (Supplementary Figure 1). We measured the amplitudes of the H^+ currents induced by serial concentrations of BAM15 and FCCP across the IMM of cardiac mitochondria (Fig. 1B-G) [11]. We recorded H^+ currents at concentrations of FCCP as low as 25 nM, while much higher concentrations of BAM15 were required to elicit measurable currents (Fig. 1B-E). At 250 nM, FCCP evoked a H^+ current with an amplitude three times higher than that measured with application of the same concentration of BAM15 (Fig. 1B-E). Based on these measurements, we determined that a BAM15 concentration approximatively 2.5 times greater was required to induce similar H^+ currents to those induced by FCCP. For example, 500 nM and 5 μM of BAM15 induced H^+ currents with amplitudes similar to those generated by 200 nM and 2 μM of FCCP, respectively (Fig. 1B-G). These concentrations were used in our further experiments to study the effects of BAM15 and FCCP on the pH of the mitochondrial matrix.

3.2. Acidification of the mitochondrial matrix due to BAM15-induced H^+ current across the IMM promotes re-alkalinization

To characterize the influence of AAC on the H^+ flux across the IMM in intact cells, we investigated the effects of the uncouplers on the matrix pH using real-time mitochondrial pH imaging. For this analysis, we used the fluorescent indicator SE-pHluorin targeted to the mitochondrial matrix of intact C2C12 cells (Fig. 2, Supplementary Figure 2) [59]. Cells were individually imaged 36–48 h after transfection with the mitochondrial matrix SE-pHluorin sensor (Fig. 2A, top panel, and B). The traces generated during the experiments were recorded as 535/480 nm emission ratios as a function of time (Fig. 2C). To estimate the changes in the matrix pH under various experimental conditions, the ratio values could be compared to the calibration curve established using the mitochondrial uncoupler FCCP to induce H^+ flux across the IMM (Fig. 2C and D, Supplementary Figure 2).

Addition of 500 nM BAM15 on intact wild-type (WT) C2C12 cells induced changes in mitochondrial matrix pH that were characterized by an acidification phase followed by a phase of re-alkalinization (Fig. 3A). To describe the relationship between the two phases in a simple manner, we first fitted the experimental data to a sum of an exponential and a sigmoidal function (Fig. 3B-D). Although not perfect, this simple model could fit most of the changes in pH and highlighted a close relationship between the exponential fit, corresponding to the acidification phase, and the sigmoidal fit for the phase of re-alkalinization. This relationship between the two components is best illustrated by the deconvolution of the fit (Fig. 3D). Those fits illustrate the correlation that exists between the time course (Fig. 3E) and the amplitude (Fig. 3F) of the acidification and alkalinization phases, with the alkalinization phase being slightly delayed relative to the acidification phase (Fig. 3D). However, this simple model provided only a partial fit of the data in other cell recordings, including the one shown in Fig. 3A, as it was challenging to fit at the same time the fast "hump" at the beginning of the re-alkalinization phase and the final slow phase of acidification (Fig. 3B). To obtain a better fit of the data, it was necessary to use the sum of two exponential functions and a sigmoidal function, underlying a mechanism with a fast (40 ≈τs) and a slow (280 ≈τs) phase of acidification and one phase of re-

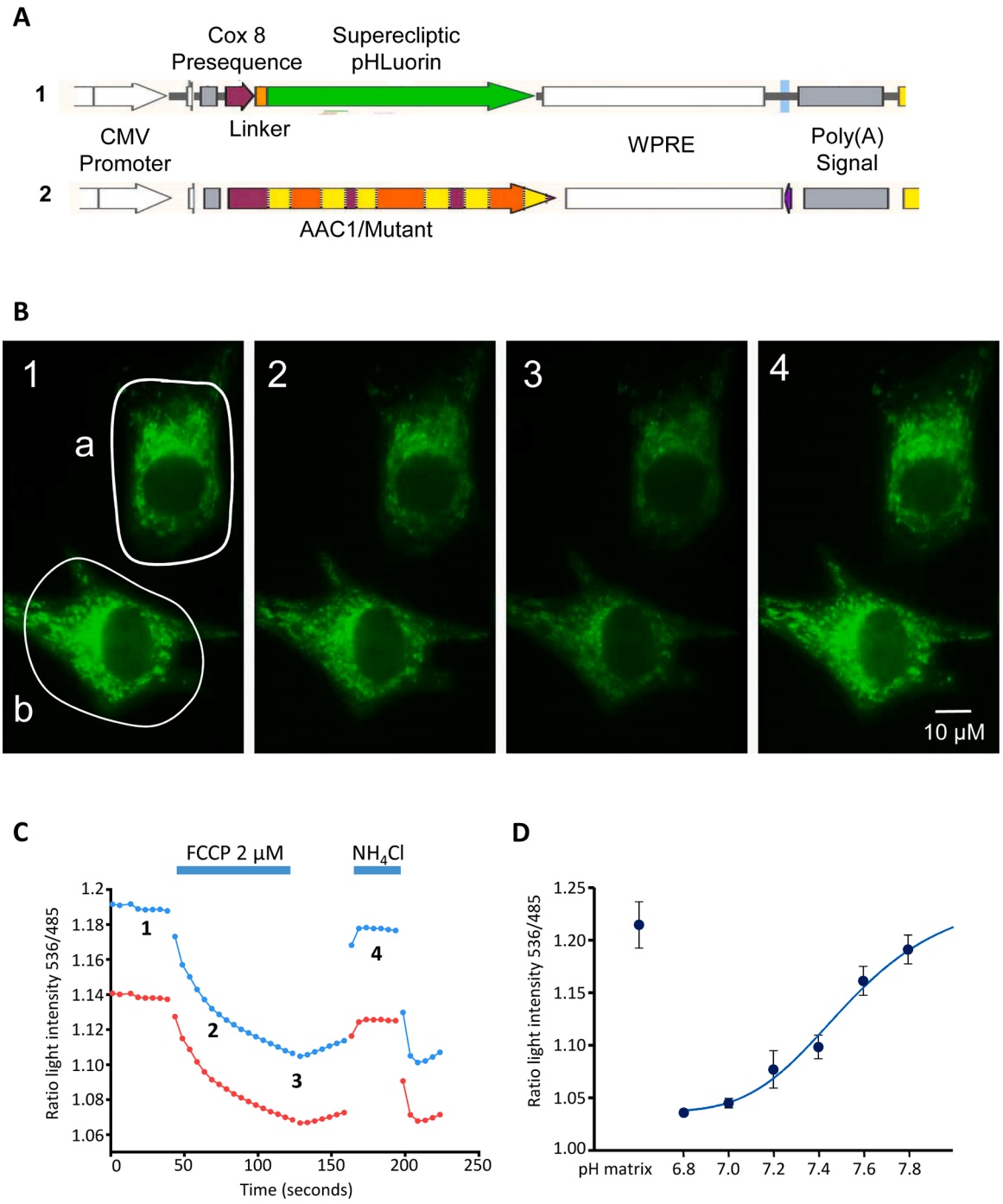

Fig. 2. Mitochondrial pHluorin expression to evaluate the mitochondrial matrix H^+ pool. A1. Generation of a Super-Ecliptic pHluorin sensor (SE-pHluorin) targeted to the mitochondrial matrix. The Cox8 SE-pHluorin coding region and WPRE non-coding region used to enhance RNA expression and stability, were removed by *Bam*HI -*Xho*I digestion of the Addgene plasmid 58500 (Venkatachalam V, Cohen AE, 2014) and inserted into a homemade plasmid (Calmettes et al., JGP 2013; John et al., PlosOne 2023), which contained the CMV promoter. A2. The same vector was used to generate the AAC1 and AAC1 A123D mutant constructs. B. Representative images of the changes in fluorescence induced by addition of 2 µM FCCP in WT C2C12 cells. In most experiments, we only recorded the ratio values shown in panel C and did not acquire images. Each experiment included measurements taken simultaneously from 2 to 5 individual cells in the same field of view. A region of interest (ROI) was drawn around each cell, and fluorescence ratios were recorded in real time from these ROIs. Upon addition of FCCP, between image #1 and image #3, a decrease in the fluorescence ratio from 1.19 to 1.15 was observed. Following removal of FCCP, addition of 20 mM NH_4Cl induced recovery of the fluorescence ratio (image #4), corresponding to re-alkalinization of the matrix (increase in light intensity). C. Representative traces of the fluorescence ratio integrated over the ROI in each cell (shown in panel B), with varying expression levels of SE-pHluorin (a, b), and changes upon addition of FCCP and NH_4Cl. The 535/480 nm emission ratio is plotted as a function of time. A downward trend of the ratio corresponds to a decrease in matrix pH, and an upward trend indicates an increase in pH. These 535/480 ratio values were recorded and used for further analysis. The level of pH sensor expression may affect the absolute value of the emission ratio (compare traces a and b), but the time course of the changes in emission ratio remains the same. This suggests that the pH sensor does not have a strong effect in buffering the matrix pH. The numbers shown along the traces (1−4) correspond to the image number in panel B. D. Changes in the emission ratio as a function of pH and fit of the data using a Hill equation. The C2C12 cells used to generate this calibration curve were first permeabilized with 100 µM β-escin and then exposed to solutions with varying pH values. The fit yielded a $pH_{0.5}$ of 7.49, consistent with that obtained by others in permeabilized cells [12]. These ratio values can

be used to estimate changes in pH in the matrix under different experimental conditions. More details on this dose-response curve are presented in Supplementary Figure 2.

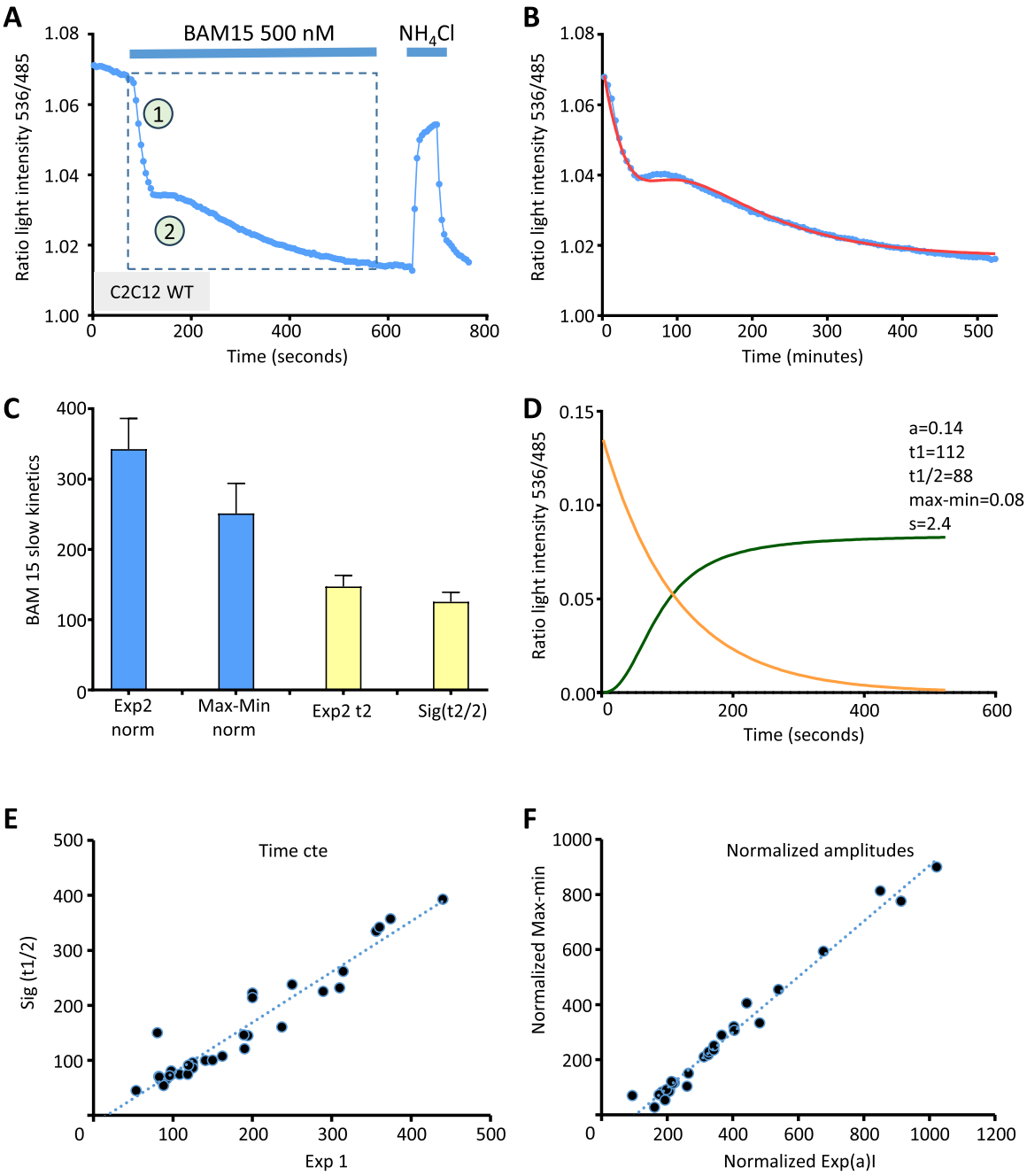

Fig. 3. Mitochondrial matrix acidification due to BAM15 induces alkalinization. A. Representative time course of the changes in fluorescence evoked by 500 nM BAM15 in WT C2C12 cells expressing SE-pHluorin targeted to the mitochondrial matrix. Addition of BAM15 evoked an initial phase of acidification that was followed by a phase of re-alkalinization. Number 1 corresponds to the acidification phase, and number 2 corresponds to the re-alkalinization phase. 20 mM NH_4Cl was added at the end of each experiment to validate the measurements and for data normalization. n = 9. B. Fit of the experimental data in panel A (dotted box), using the sum of an exponential and a sigmoidal function. The blue dots are the experimental data, and the red line corresponds to the fit. C. Bar graph showing the correlation between the amplitude and time course of the exponential and sigmoidal functions. Mean ± s.e.m. n = 31 (BAM15 100 nM: n = 4, BAM15 500 nM: n = 9, BAM15 5 μM: n = 18). D. Deconvolution of the fit in B into its two components. The orange trace corresponds to the acidification phase, and the green trace corresponds to the re-alkalinization phase. Note the same time scale is used in panels B and D. This analysis shows that the fluorescence changes induced by BAM15 comprise an exponential acidification that triggers a sigmoidal re-alkalinization phase. E. Correlation between the acidification time constant and the halfway point of the re-alkalinization phase. n = 31 (BAM15 100 nM: n = 4, BAM15 500 nM: n = 9, BAM15 5 μM: n = 18). F. Correlation between the amplitude of the exponential phase and the difference between the maximum and minimum of the sigmoid. n = 31 (BAM15 100 nM: n = 4, BAM15 500 nM: n = 9, BAM15 5 μM: n = 18).

alkalinization (Supplementary Figure 3A-G). Based on the latter fit, we hypothesized that the initial fast exponential phase of acidification corresponds to the AAC-dependent H^+ current (Supplementary Figure 3D and G), while the slow exponential phase of acidification corresponds to the protonophoric activity of BAM15 (Supplementary Figure 3 F and G). Thus, while it was possible to separate a fast phase and a slow phase of acidification in some cells, this was not always the case. Indeed, in many instances this distinction was not feasible, as the

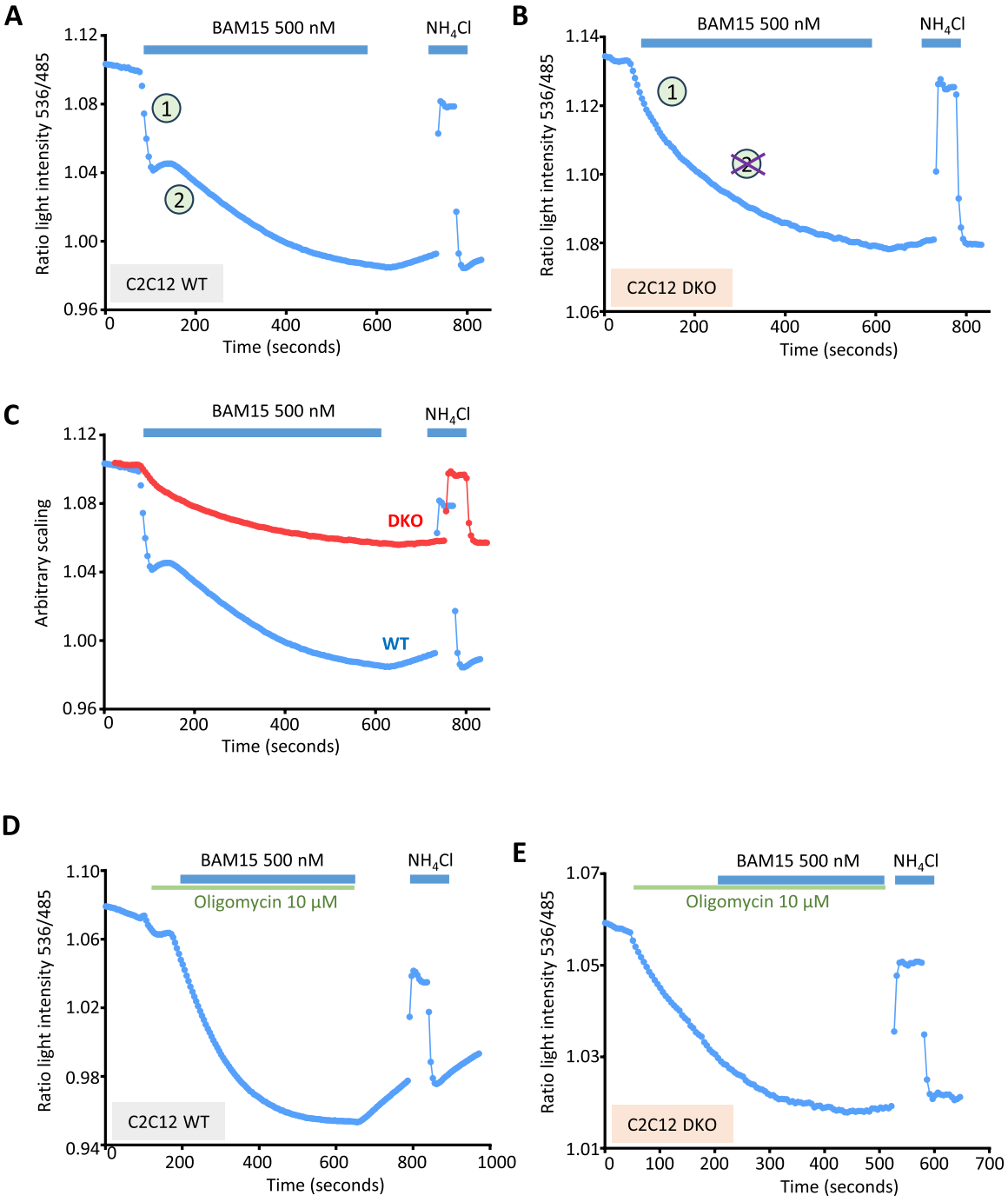

Fig. 4. BAM15 induces H^+ fluxes across the IMM that rely on AAC and the ATP synthase. A. Representative time course of the changes in fluorescence evoked by 500 nM BAM15 in WT C2C12 cells expressing SE-pHluorin targeted to the mitochondrial matrix. This caused acidification of the matrix (phase 1) followed by a phase of alkalinization (phase 2). n = 9. B. Representative time course of fluorescence changes induced by 500 nM BAM15 in DKO C2C12 cells expressing SE-pHluorin. BAM15 induced a slow acidification phase but no re-alkalinization phase. n = 18. C. Superimposition of traces shown in panels A and B to illustrate the evolution over time of fluorescence changes caused by 500 nM BAM15 in WT (A) and DKO (B) cells. This superimposition shows that the acidification phase caused by BAM15 is faster in WT cells than in DKO cells when acidification is adjusted to a single exponential. However, with the use of a two-time-constant exponential adjustment for acidification in WT cells, the values are comparable to those obtained with DKO cells, 31.85-/280.57 + =τ (n = 10) for WT cells and 235.33 + =τ/-49 (n = 18) for DKO cells. The Y-axis represents arbitrary units. D. Representative time course of the changes in SE-pHluorin fluorescence in WT C2C12 cells elicited by 500 nM BAM15 after pretreatment with 10 µM oligomycin. n = 11. E. Time course of the changes in SE-pHluorin fluorescence in DKO C2C12 cells elicited by 500 nM BAM15 after pretreatment with 10 µM oligomycin. n = 9. 20 mM NH_4Cl was added at the end of each experiment to assess the responsiveness of the sensor and for normalization of the data.

fast phase of acidification (AAC-dependent H^+ current) and the slow phase of acidification (protonophoric current) may have had similar slow kinetics. In this case, a single exponential phase of acidification with a 140 ≈τs was sufficient to obtain a good fit of the data (Supplementary Figure 4).

Although a more complex double exponential fit would describe the two acidification phases more accurately, we used the simpler model (an exponential function plus a sigmoidal function) for most analyses, as it

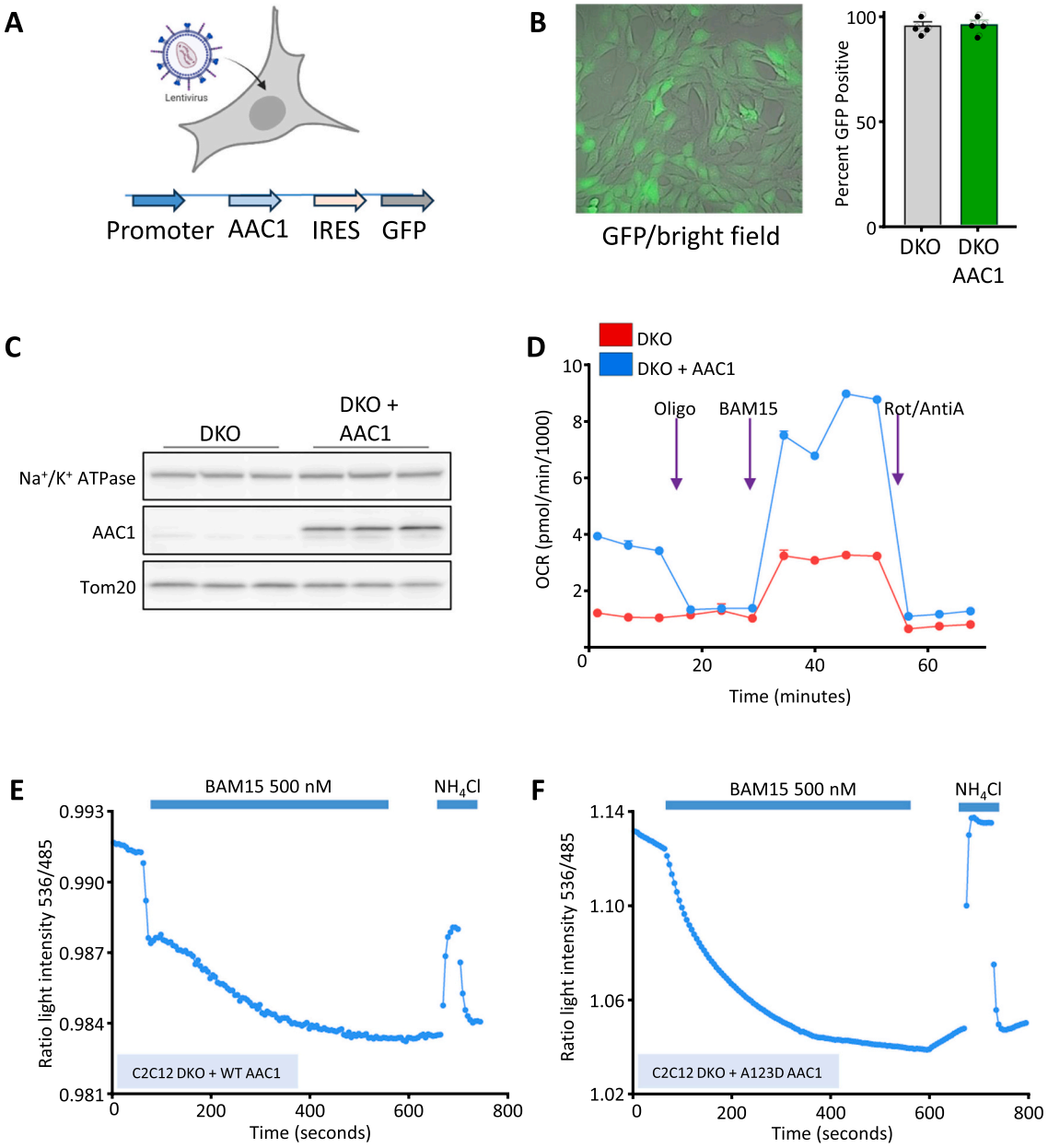

Figure 5. Reintroduction of functional AAC1 in DKO C2C12 cells re-establishes the re-alkalinization phase. **A.** Diagram of the lentivirus vector used to reintroduce mouse AAC1 in DKO C2C12 cells. A bicistronic construct was used to express AAC1 and GFP together and avoid tagging AAC1. **B.** Left panel: Representative bright field image overlaid with a GFP fluorescent image showing that about 95 % of C2C12 DKO cells were GFP positive. Right panel: quantification of GFP-positive cells among DKO cells transduced with cytosolic GFP as a control (grey bar) and DKO cells transduced with the bicistronic construct AAC1 (green bar). Data are mean ± s.e.m. n = 4 coverslips per condition. **C.** Western blot analysis of total cell extract protein marker, Na^+/K^+ ATPase, AAC1, and mitochondrial biomass marker TOM20 expression. AAC1 was only detected after it had been reintroduced via lentivirus transduction. n = 3 per group. **D.** DKO C2C12 cells (red line) developed a very small OCR, for which oligomycin application had no effect. BAM15 induced OCR due to its protonophoric activity. OCR was reduced in the absence of AAC, but with AAC1 reintroduction (blue line), basal respiration was recovered and oligomycin reduced OCR. These data demonstrate that the ADP/ATP exchange is functional with the reintroduced AAC1. The maximal respiration also increased with the application of BAM15 injection. AAC1 was thus capable of both its functions, ADP/ATP exchange and H^+ transport. Data are mean ± s.e.m. n = 13 wells for DKO and DKO+AAC1. See Supplementary Figure 5 for OCR data interpretation. **E.** Representative time course of the changes in SE-pHluorin fluorescence evoked by BAM15 in DKO C2C12 cells in which AAC1 had been reintroduced. For these experiments, the cells were transfected with the two plasmids for WT AAC1 and SE-pHluorin. Both phases, acidification and re-alkalinization, were observed, demonstrating that AAC1 is required for the re-alkalinization phase. n = 12. **F.** Representative time course of the changes in SE-pHluorin fluorescence evoked by BAM15 in DKO C2C12 cells expressing the non-functional A123D AAC1 mutant. For these experiments, cells were transfected with the two plasmids for A123D AAC1 and SE-pHluorin. Under these conditions, an acidification phase was elicited by BAM15, but no re-alkalinization phase was observed. n = 11. 20 mM NH_4Cl was added at the end of each experiment to assess the responsiveness of the sensor and for data normalization.

was not possible to separate the two acidification phases when the initial acidification was relatively slow (50 ≥τs) and was close to the value of the slow acidification time constant (200 s) (see the Methods section for further explanation). Furthermore, for our purposes, the simple exponential fit provided a satisfactory interpretation of the relationship between the acidification and re-alkalization phases.

3.3. Re-alkalinization of the matrix following its acidification requires both functional AAC and the ATP synthase

We next studied the effect of AAC removal on the changes in the matrix pH evoked by the uncoupler BAM15 in DKO C2C12 cells. We found a phase of acidification in the absence of AAC but no phase of re-alkalinization compared with the recordings from WT cells (Fig. 4A and B). The former was sustained and slow, and likely due to the protonophoric activity of BAM15 (Fig. 4B). These observations indicate that: i) AAC is required for the BAM15-induced re-alkalization following the initial acidification, and ii) a slow kinetics phase of acidification is still induced by BAM15 in DKO cells, which is very likely due to its protonophoric activity [11]. It should be noted that in DKO cells, the average acidification time constant was 235.33 ± 49 (n = 18) and was comparable to the value of 280.57 ± 31.85 (n = 10) obtained with the two-exponential fit (Supplementary Figure 3). The acidification phase induced by BAM15 in C2C12 DKO cells was slower than that observed in WT cells, as clearly illustrated by the superimposition of the two conditions (WT and DKO traces, Fig. 4C). This is probably due to a delay in the slow acidification phase contaminated by the initial rapid acidification phase in DKO cells.

We then hypothesized that the re-alkalinization phase is due to H^+ extrusion from the matrix due to the reversed activity of the ATP synthase [20,43]. Under these conditions, the ATP synthase may hydrolyze ATP produced via glycolysis, which is likely imported by AAC from the cytosol into the mitochondrial matrix [20,3,50,60]. Such a mechanism would be consistent with a functional interaction between AAC and the ATP synthase that would facilitate re-alkalinization [33,60]. To ascertain the role of the ATP synthase in this process, we investigated how BAM15-mediated changes in the matrix pH were affected by treatment of WT C2C12 cells with the ATP synthase inhibitor oligomycin (Fig. 4C). We first exposed the cells to oligomycin for about 30 s and then applied BAM15. The addition of oligomycin did not prevent the acidification evoked by BAM15, but it completely blocked the re-alkalinization phase, suggesting that the ATP synthase is involved in the mechanism responsible for the re-alkalization process (Fig. 4D). We also investigated how oligomycin may modulate the effect of BAM15 in DKO C2C12 cells. Contrary to what was observed with WT C2C12 cells, the addition of oligomycin in DKO C2C12 cells caused a gradual and sustained acidification of the matrix. Furthermore, addition of BAM15 under these conditions had no further effects on the pH of the matrix (Fig. 4E). The lack of effect of BAM15 was independent of the time of application after starting the treatment with oligomycin. Thus, it appears that in DKO cells, inhibition of the ATP synthase causes an acidification of the matrix, and this effect blocks the pH lowering effect of BAM15.

Together, these observations suggest that a functional AAC-dependent transport of ADP and ATP across the IMM must be operational to enable the extrusion of H^+ from the matrix to the intermembrane space via the ATP synthase [33,57,60].

3.4. AAC is essential for the re-alkalinization phase induced by BAM15

To confirm that AAC is essential for the re-alkalinization phase, we reintroduced AAC1, the main isoform in heart and skeletal muscle, into the DKO C2C12 cells (Fig. 5).

To ascertain that the reintroduction of AAC1 in DKO C2C12 cells could indeed recapitulate a WT mitochondrial phenotype, we first created a stable cell line expressing AAC1 (Fig. 5A and B). We found a detectable level of AAC1 protein in DKO cells in which AAC1 had been reintroduced but not in DKO cells treated with empty vector (Fig. 5C). We then use cellular respirometry to confirm that the added AAC1 was functional for its two transport modes, ADP/ATP exchange and H^+ current (Supplementary Figure 5). The mitochondrial oxygen consumption rate (OCR), which is modulated in part by the flux of H^+ across the IMM, can be used as a readout of AAC activity. In DKO cells, the basal OCR measurement was greatly reduced, indicating the absence of ADP/ATP exchange. Under these conditions, addition of oligomycin had no effect (Fig. 5D, Oligo). It should be noted that BAM15 could still induce some limited OCR in the DKO cells, possibly due to its protonophoric activity. When WT AAC1 was reintroduced into DKO C2C12 cells, the basal respiration level was higher, and oligomycin treatment inhibited the respiration. ATP synthesis activity was also recovered, demonstrating that our exogenous WT AAC1 functions as an ADP/ATP exchanger. The finding that BAM15 treatment also increased the OCR after reintroduction of AAC1, suggests that AAC-dependent H^+ transport was operational. It should be noted that the reintroduction of AAC1 resulted in only partial recovery, as AAC did not reach the levels observed in WT cells, which express both the AAC1 and AAC2 isoforms at the myoblast stage. We used two lentivirus titers, MOI1 (x1) and MOI5 (x5) to reintroduce AAC1 in the DKO C2C12 cells. With MOI1, the level of AAC1 protein was approximately 17 % of the total amount of AAC1/AAC2 protein found in WT cells (Supplementary Figure 6 A and B). With the higher lentivirus titer (MOI5, x5), the amount of AAC1 protein expression was even lower, reaching approximately 5 % of the total amount of AAC1/AAC2 protein found in WT cells. Although reintroduction was partial, the OCR level reached with the AAC1 x1 group was approximately 55 % of that measured in the control WT C2C12 cells and 36 % of control with the AAC1 x5 group (Supplementary Figure 6 C). Furthermore, mitochondrial ATP production (ATP OXPHOS) recovered by more than half in both groups compared to WT and was not detectable in the DKO (Supplementary Figure 6D).

To summarize, AAC1 that we reintroduced in DKO C2C12 cells exhibited the canonical ADP/ATP exchange and H^+ current transport modes. Even though its reintroduction in DKO C2C12 cells at the protein level was only partial, it recapitulated the standard respiratory profile with normal ATP synthase and thermogenesis functions.

Once we determined that the reintroduced AAC1 was functional, we overexpressed it together with the pH indicator SE-pHluorin in DKO C2C12 cells at a 1:1 ratio. We also reintroduced the non-functional AAC1 mutant for ADP/ATP exchange (A123D AAC1), which has been previously described as a loss-of-function mutation associated with mitochondrial myopathy and cardiomyopathy in humans [44,45]. As mentioned previously, addition of 500 nM BAM15 in DKO C2C12 cells induced an acidification phase but no phase of re-alkalinization (Fig. 4B). Consistent with our earlier observations, we found that when WT AAC1 was reintroduced in DKO C2C12 cells via either co-expression of separate AAC1 and SE-pHluorin genes or expression of AAC1 and SE-pHluorin in an internal ribosome entry site (IRES) vector, BAM15 induced a re-alkalinization phase following the initial phase of acidification (Fig. 5E). In contrast, BAM15 did not evoke any phase of re-alkalinization in response to the acidification when the A123D AAC1 mutant was introduced in the DKO C2C12 cells (Fig. 5F).

These results confirm our hypothesis that the re-alkalization phase results from the reverse activity of ATP synthase and that functional AAC1 regulates this process. It remains to be determined whether, in this case, AAC also functions in reverse to supply cytosolic ATP to ATP synthase [16,20,58].

3.5. The re-alkalinization phase is regulated by the AAC-dependent H^+ current and not by the protonophoric current

Our next step was to assess the respective roles of the AAC-dependent H^+ current and of the protonophoric current in regulating ATP synthase in its reverse mode. To this end, we took advantage of the different properties of the currents evoked by BAM15 and FCCP, which in the

former case is primarily carried by AAC, while being 50 % protonophoric in the case of FCCP (Fig. 1A and H).

We first investigated the effects of 500 nM and 5 μM BAM15 on WT C2C12 cells. With both concentrations, the changes in mitochondrial matrix pH were characterized by an acidification phase, which appeared to be closely linked to a phase of re-alkalinization (Fig. 6A and B). Next, we compared the effects of FCCP with those of BAM15 at different concentrations. Although 200 nM FCCP induced the typical acidification/re-alkalinization pattern observed with BAM15, 2 μM FCCP did not elicit a phase of re-alkalinization despite the activation of an acidification phase (Fig. 6C and D). We even tried a lower concentration of FCCP (75 nM, Fig. 6E), which resulted in a well pronounced re-alkalinization phase (Fig. 6E). Thus, while 5 μM BAM15 and 2 μM FCCP generated H^+ currents of similar amplitude across the IMM

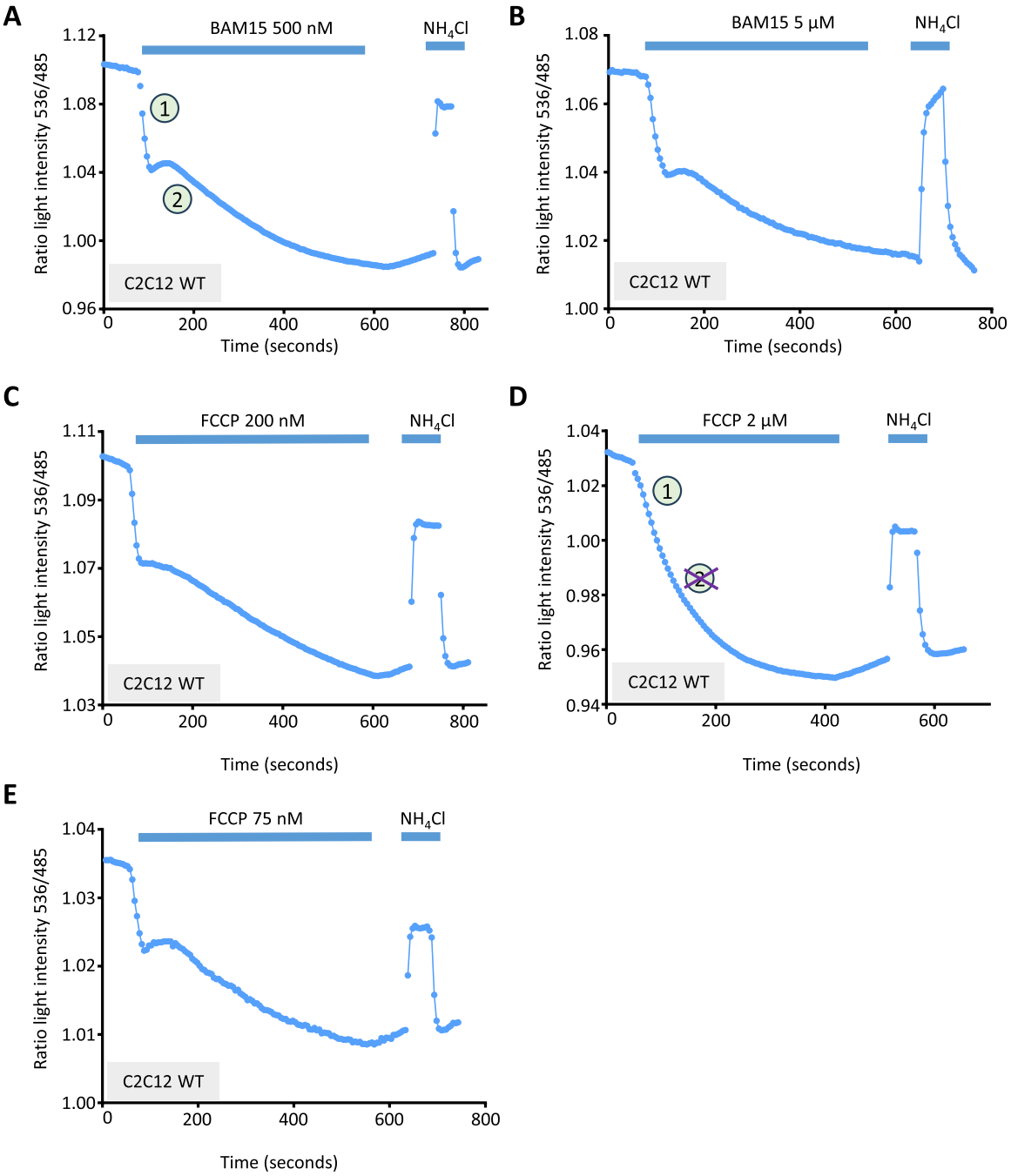

Fig. 6. Differences in mitochondrial pH profile with BAM15 and FCCP treatment. A. Representative time course of the changes in fluorescence evoked by 500 nM BAM15 in WT C2C12 cells expressing SE-pHluorin targeted to the mitochondrial matrix. This caused acidification of the matrix (phase 1), followed by a phase of alkalinization (phase 2). n = 9. **B.** Representative time course of the changes in fluorescence evoked by 5 μM BAM15 in WT C2C12 cells expressing SE-pHluorin. At this concentration, BAM15 still elicited acidification of the matrix, followed by re-alkalinization. n = 18. **C.** Representative time course of the changes in fluorescence evoked by 200 nM FCCP in WT C2C12 cells expressing SE-pHluorin. At this concentration, FCCP was able to elicit acidification of the matrix, which was followed by a re-alkalinization. n = 12. **D.** Representative time course of the changes in SE-pHluorin fluorescence in WT C2C12 cells after addition of 2 μM FCCP. At this concentration, FCCP could still elicit acidification of the matrix, but the phase of re-alkalinization was no longer present. n = 18. **E.** Representative time course of the changes in SE-pHluorin fluorescence in WT C2C12 cells after addition of 75 nM FCCP. n = 4. 20 mM NH_4Cl was added at the end of each experiment to assess the responsiveness of the sensor and for data normalization.

(Fig. 1B-G), the resulting changes in pH in the mitochondrial matrix differed. We hypothesized that the difference in response to BAM15 and FCCP, i.e., the lack of re-alkalinization with high concentrations of FCCP, is because most of the H^+ current induced by BAM15 is mediated via AAC, when the amplitude of the protonophoric current remains small even at high concentrations of BAM15. However, this is not the case with FCCP; instead, increased acidification due to large protonophoric currents evoked by high concentrations of FCCP may overcome any possible re-alkalinization of the matrix, rendering the reverse activity of the ATP synthase irrelevant [11].

We postulate based on these data that the phase of re-alkalinization may be linked to the acidification due to H^+ current flowing through AAC and not by the protonophoric current (AAC-independent).

3.6. *Inhibition of ETC activity induces similar acidification/re-alkalinization profiles*

We presented in Sections 3.2 and 3.3 that: i) acidification of the matrix by the BAM15-dependent H^+ current caused an acidification phase followed by a re-alkalinization phase (Fig. 3A); ii) in DKO C2C12 cells, BAM15 induced acidification but not alkalinization (Fig. 4B); and iii) oligomycin blocked the alkalinization following the acidification

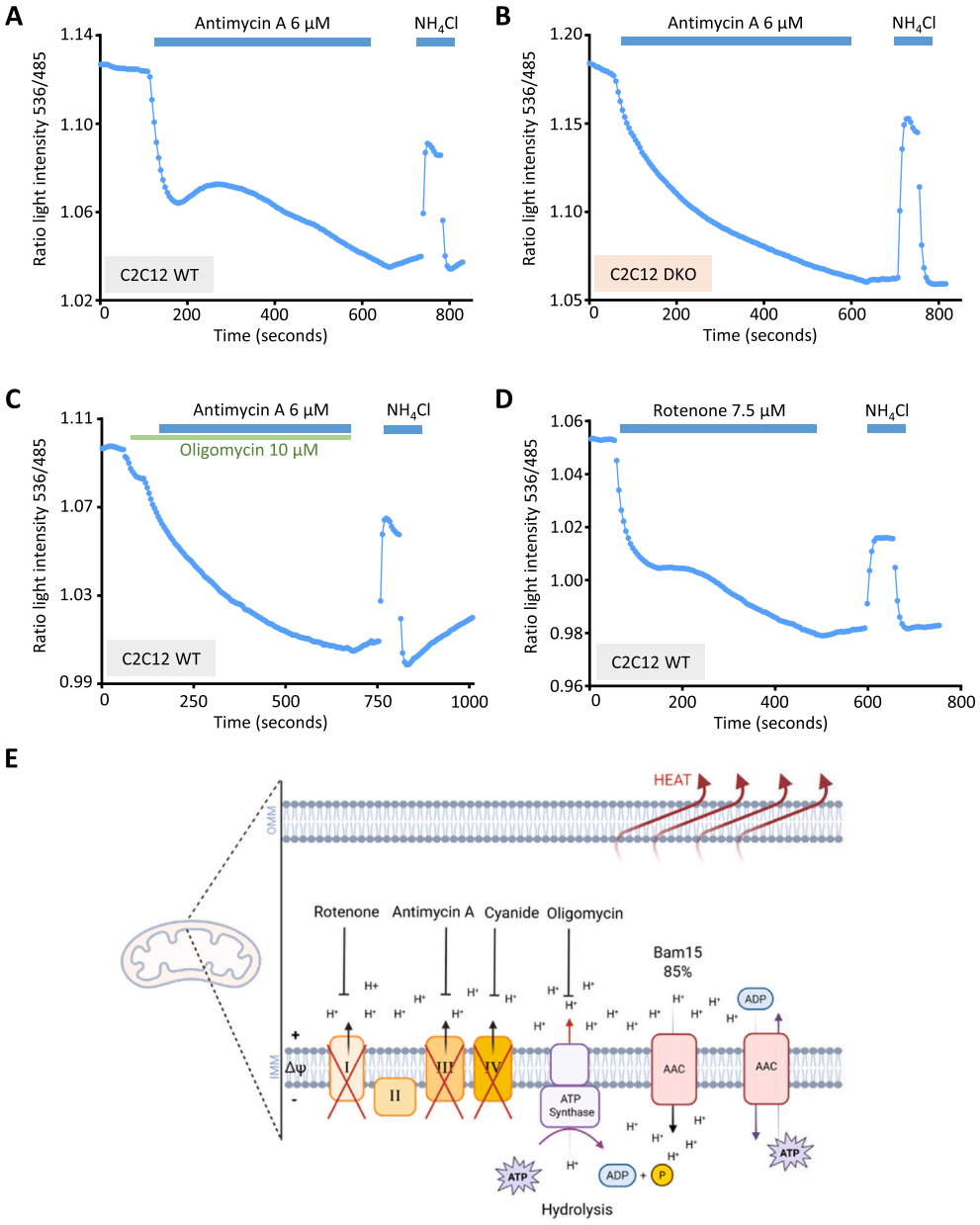

Fig. 7. H^+ accumulation in the matrix due to ETC inhibition leads to the ATP synthase reversal activity. A. Representative time course of the changes in SE-pHluorin fluorescence evoked by 6 µM antimycin A in WT C2C12 cells. Antimycin A induced acidification of the matrix, followed by a phase of re-alkalinization, as observed with BAM15 treatment. n = 53. B. Representative time course of the changes in SE-pHluorin fluorescence evoked by 6 µM antimycin A in DKO C2C12 cells. In these cells, antimycin A induced a phase of acidification but no phase of re-alkalinization. n = 25. C. Representative time course of the changes in SE-pHluorin fluorescence evoked by 6 µM antimycin A in WT C2C12 cells after pretreatment with10 µM oligomycin. Under these conditions, an acidification phase occurred, but inhibition of the ATP synthase activity blocked the phase of re-alkalinization. n = 21. D. Representative time course of the changes in SE-pHluorin fluorescence evoked by 7.5 µM rotenone in WT C2C12 cells. Rotenone induced acidification of the matrix, followed by a re-alkalinization phase, similar to that observed with antimycin A. n = 11. E. Diagram representing each mitochondrial compound target. 20 mM NH_4Cl was added at the end of each experiment to assess the responsiveness of the sensor and for data normalization.

phase evoked by BAM15 (Fig. 4C). Based on these observations, we hypothesized that the alkalinization phase was due to an efflux of H^+ through the ATP synthase caused by the activity of AAC-dependent H^+ transport, leading to an increase in the H^+ level in the mitochondrial matrix.

We then examined whether acidification of the matrix by a different process, i.e., inhibition of ETC, could induce an acidification/re-alkalinization process similar to that observed with BAM15. Notably, the transport of H^+ through the ETC is highly regulated and has a strict stoichiometry [46], and inhibition of the ETC has been previously linked to the reversal activity of the ATP synthase [2,43]. In the present study, cells treated with either antimycin A (Fig. 7A), an inhibitor of complex III, or rotenone (Fig. 7D), an inhibitor of complex I, exhibited acidification/alkalinization patterns similar to those induced by BAM15 (Fig. 3). Comparison of the time courses of the "slow" phase of acidification induced by BAM15, FCCP and antimycin A revealed slight differences (Supplementary Figure 8). In DKO C2C12 cells, antimycin A evoked an acidification phase but no alkalinization phase (Fig. 7B). Finally, preincubation of WT cells with oligomycin blocked the effect of antimycin A on the re-alkalinization phase (Fig. 7C). These observations are important in many aspects and show that: i) the elevation of H^+ concentration in the matrix that activates the re-alkalinization phase is not specific to the entry of H^+ via AAC; ii) the presence and activity of AAC to likely transport ATP into the matrix is still necessary for the re-alkalinization phase to develop in the presence of antimycin A and; iii) the functional interaction of ADP/ATP exchange by AAC with the ATP synthase is necessary for this process to take place.

Notably, the effects of NaCN were similar but not as pronounced as those of antimycin A, perhaps due to a lesser acidification of the matrix evoked by the inhibitor (Supplementary Figure 7). Indeed, as with antimycin A, addition of NaCN caused an acidification phase that was followed by a re-alkalinization phase (Supplementary Figure 7 A), and preincubation with oligomycin blocked the phase of re-alkalinization (Supplementary Figure 7B).

4. Discussion

The present study provides the first characterization of a functional interaction between AAC-dependent H^+ transport and the reverse activity of the ATP synthase in a myoblast cell line using real-time imaging with the SE-pHluorin pH sensor targeted to the mitochondrial matrix to measure changes in matrix pH.

4.1. H^+-dependent functional interaction between AAC and the ATP synthase in C2C12 cells

Our initial goal was to determine the effect of AAC-dependent H^+ current on mitochondrial matrix pH as an indicator of H^+ flux across the IMM. Due to the rapid, dynamic, and molecular nature of H^+ flux across the IMM, the use of a pH probe expressed in the mitochondrial matrix was mainly accessible in cell lines. We previously generated a double knockout of the AAC1 and AAC2 isoforms in the C2C12 myoblast cell line to provide a genetic tool to confirm the primary contribution of AAC to mitochondrial uncoupling [9]. We chose a myoblast cell line to be consistent with our experiments using the *AAC1*$^{-/-}$ mouse model [9]. Although expressed in most tissues, AAC1 is the main AAC in the heart and skeletal muscles [15,36]. AAC2 is also expressed in the heart and skeletal muscles at low levels, but it is highly expressed in a myoblast cell state [28]. We therefore created a double knockout for both isoforms. We have previously characterized the C2C12 WT and DKO cells extensively to validate their suitability and study their mitochondrial morphology, OXPHOS profile, mitochondrial biomass, and respiratory capacity. We have made these cells our primary model for studying AAC on this basis [11,7].

Because most (85 %) of the current induced by BAM15 is due to AAC in heart mitochondria and C2C12 cells, it is an excellent pharmacological tool for studying AAC-dependent H^+ current in a cellular context [11]. This is the first time we have been able to pharmacologically induce AAC to transport H^+ in a controlled manner and study its impact on matrix pH dynamics in cells using a pH probe. One of the novelties of the present work is the use of pharmacological tools to study the role of AAC in H^+ transport and energy distribution by mitochondria. It is still assumed that BAM15 acts primarily as a protonophore, even though we have found that AAC is the main target for BAM15 in heart and C2C12 cells [11]. Consequently, we hypothesize that, because most cells strongly express AAC, there is a high probability that BAM15 uncouples mitochondria via AAC in most cell types. However, this has not yet been proven, and we hope to be able to answer this question in the future.

Our matrix pH experiments demonstrated that BAM15 induces an acidification phase that is associated with a re-alkalinization phase in C2C12 cells. Analysis of the data showed a close temporal relationship between the two phases (Fig. 3). In addition, we demonstrated that the acidification phase is linked to AAC and that the re-alkalinization phase requires the reverse activity of the ATP synthase (Fig. 4). Indeed, DKO C2C12 cells and the use of the ATP synthase inhibitor oligomycin blocked the re-alkalinization phase.

We showed that overall, the sum of exponential and sigmoidal functions fit well the acidification and re-alkalinization phases (Fig. 3B). However, such a simple fit did not explain the data when the acidification and alkalinization phases were rapid (40 ≈τs; Supplementary Figure 3). In this case, the fit required two exponential functions and one sigmoidal function, and the time course and amplitude of the fast exponential function (acidification) were closely related to the time course and amplitude of the sigmoidal function (re-alkalinization). In the absence of AAC, the acidification phase was slow and did not induce any re-alkalinization phase. These findings indicated that the fast acidification phase depends on AAC and is responsible for the re-alkalinization phase. As a corollary, the slow acidification phase (slow exponential time constant), which did not cause a phase of re-alkalinization, is likely due to the protonophoric activity of the chemical uncoupler.

Comparison of the two pH measurement curves in Supplementary Figures 3 A and 4 A reveals two different time constants for the "fast" acidification phase, respectively 40 ≈τs and ≈ 180 s. Yet, both acidification phases triggered a re-alkalinization phase. Given these data, we wondered whether there is a continuum of the acidification phases from fast to slow. This does not appear to be true, as both types of phases could be detected simultaneously and were associated in both cases with re-alkalinization phases (Supplementary Figure 4D). Although rare, such differences suggest that fast and slow acidification/re-alkalinization processes represent distinct functional interactions between AAC and the ATP synthase in C2C12 cells, possibly linked to two different compartments.

4.2. ATP-dependent regulation of the ATP synthase by AAC

Because acidification of the matrix due to H^+ entry via AAC could trigger a re-alkalinization phase in C2C12 cells, we hypothesized that AAC tightly controls the balance of H^+ across the IMM. Interestingly, inhibition of the ETC, which induced acidification independently of AAC-dependent H^+ current, also resulted in a re-alkalinization phase (Fig. 7). Furthermore, the re-alkalinization phase induced by the ETC inhibitors involved AAC, as it could not develop in DKO C2C12 cells (Fig. 7C). These results are important as they strongly suggest that the role of AAC in the process of re-alkalinization is mediated not only via its ability to carry H^+ but also its ADP/ATP exchange function. Considering that acidification of the mitochondrial matrix, whether due to H^+ entry via AAC or blocking of H^+ efflux by ETC inhibition, requires AAC, our results suggest that the re-alkalization phase is due to the reverse activity of the ATP synthase, which involves ATP hydrolysis [20,43,60]. In our experiments, oligomycin blocked the re-alkalization phase induced

by either BAM15 or ETC inhibitors (Figs. 4F and 7C), confirming that the ATP synthase is responsible for H^+ extrusion when functioning in reverse, a process likely dependent on the ATP supply provided by AAC [16,20,58].

To further investigate whether ADP/ATP exchange via AAC is necessary for the activation of the ATP synthase in the reversed mode, we reintroduced the AAC1 A123D mutant, a well-characterized mutant lacking ADP/ATP exchange capacity, which is still expressed at the IMM [44,45], into DKO C2C12 cells. Unlike the reintroduction of WT AAC1, which allowed for the recovery of the re-alkalization phase induced by BAM15 and antimycin A, the reintroduction of the A123D mutant did not (Fig. 5E and F). These data suggest that the reverse activity of AAC facilitates the entry of glycolytic ATP into the matrix to supply the ATP synthase [20,33] [16] [58]. To confirm that AAC does indeed work in a reverse manner to provide the ATP synthase with a higher pool of ATP in the matrix, it will be necessary to assess the levels of ATP in the mitochondrial matrix and in the cytosol using encoded biosensors and perform the same type of experiments that we used to study pH dynamics in C2C12 cells [49] [24] [62]. In this regard, it will be interesting to investigate whether depletion of cytosolic ATP occurs with both uncouplers or only with FCCP at high concentrations.

From these collective results, we propose a functional interaction between AAC and the ATP synthase, and potentially the ETC in C2C12 cells, to regulate H^+ fluxes across the IMM. This functional interaction could be related to a physical interaction between AAC and the ATP synthase, as has been suggested by previous studies. Indeed, AAC directly interacts with the ATP synthase and the inorganic phosphate carrier to form the ATP synthasome, a complex optimized for ATP production [18,34]. AAC and the ATP synthase also physically interact in their role in permeability transition pore opening [15,5,57]. Respiratory complexes CIII and CIV may act together with AAC to enhance oxidative phosphorylation, interactions that are only possible in the presence of cardiolipin [22,37,53]. Overall, direct interactions such as those between AAC and respiratory complexes and between AAC and the ATP synthase may contribute to the regulation of the H^+ flux across the IMM.

Other players, such as UCP2 and UCP3, whose involvement in mitochondrial uncoupling in non-adipose tissues has been widely reported, may participate in mitochondrial bioenergetic regulation [14,25]. Our previous experiments have shown that UCP2 and UCP3 proteins do not participate in H^+ transport in muscle mitochondria [7,10]. However, these two carriers have recently been characterized to transport C3-C4 metabolites and reported to participate in regulation of glucose and glutamine oxidation [13,14,35,41,61]. It will therefore be interesting to investigate whether UCP2 and UCP3 could support a specific metabolism required for AAC-dependent H^+ transport and thermogenesis.

4.3. Mechanism of H^+ transport by the ATP synthase and its regulation by ATP

The H^+ gradient across the IMM and the mitochondrial membrane potential are closely linked, which impacts mitochondrial bioenergetics [25,65]. Interestingly, all components that control H^+ flux across the IMM affect the maintenance of the mitochondrial membrane potential, including the reverse action of the ATP synthase, which prevents membrane depolarization when the ETC is inhibited [2,43,58]. Uncouplers are also known to induce a dissipation of the membrane potential, which also causes the ATP synthase to function in reverse [16,20,43,58]. Thus, an increase in the H^+ level in the matrix, due to either ETC inhibition or H^+ influx induction, could lead to the reversal of the electrochemical gradient across the IMM, and this may be associated with ATP hydrolysis and the reversal of the ATP synthase activity. Hydrolysis of ATP by the ATP synthase and dissipation of the membrane potential are often associated with mitochondrial pathologies, suggesting a compensatory mechanism in bioenergetics crisis conditions [2,20,3,50]. Dysregulation of the AAC-dependent H^+ flux across the IMM also was shown to be associated with aging in a model of primary cardiomyocytes [63].

It has been proposed that, to maintain mitochondrial membrane potential with a high concentration of uncoupler, AAC transports glycolytic ATP into the matrix to fuel the ATP synthase to function in reverse [16,20,58]. This could lead to energy depletion in cells if too much glycolytic ATP is used by mitochondria [20]. Our pH measurement data suggest that at low concentrations of FCCP (75–200 nM), AAC appears to be able to supply the ATP synthase with ATP and to allow IMM repolarization (re-alkalinization phase; Fig. 6C). However, at high FCCP concentration (2 μM; Fig. 7D), the re-alkalinization phase is undetectable, suggesting that the ATP synthase is no longer able to compensate for the elevated influx of H^+ across the IMM and thus for the re-alkalinization phase to occur. Regardless, AAC may still transport ATP to the ATP synthase for hydrolysis under these conditions. However, a high concentration of FCCP due to excessively powerful protonophoric activity could also inhibit mitochondrial respiration (ETC and ATP synthase activity) due to the dissipation of mitochondrial membrane potential, which in turn is essential for mitochondrial function, including the import of substrates for the Krebs cycle and ion transport (K^+, Na^+, Ca^{2+}) [26,42,54,55]. In contrast, high concentration of BAM15 (5 μM) evoked a re-alkalinization phase (Fig. 6B), even though, our electrophysiological measurements established that 5 μM BAM15 elicited H^+ currents with amplitudes similar to those induced by 2 μM FCCP (Fig. 1). Therefore, we propose that the pool of H^+ responsible for the re-alkalinization phase appears to be tightly controlled by H^+ transport via AAC, but when the protonophoric activity takes over, the re-alkalinization phase is suppressed.

As our study specifically focused on C2C12 cells, our conclusions should not be generalized to other cell types, and further research is needed to confirm the existence of such a role of AAC in cell lines other than myoblasts. Interestingly, a recent study published by the group that discovered BAM15 used mitochondrial respiration to study the effects of a number of uncouplers, including BAM15, in different cell lines representing different tissues. BAM15 had an effect on all the cells tested, with C2C12 cells (their first article) and rat L6 myoblasts exhibiting the most potent mitochondrial uncoupling capacity [32,54]. Given that all these cell lines should exhibit high levels of AAC expression, it follows that the probability of BAM15 uncoupling mitochondria in all cell lines via AAC is high. Moreover, AAC and the ATP synthase are both highly expressed in all tissues. Indeed, AAC is considered to be one the most highly expressed mitochondrial proteins (~10 % of the total amount). Although expressed in most tissues, AAC1 is the main AAC in the heart and skeletal muscles [15,36]. AAC2 is also expressed in the heart and skeletal muscles at low levels, but AAC2 is highly expressed in a myoblast cell state [15,28]. The Mitocarta inventory of mammalian mitochondrial proteins showed the distributions of AAC1 and AAC2 proteins in several mouse tissues, and in all 14 tissues tested, AAC1 and AAC2 were found at high levels. This includes four different brain parts, heart, skeletal muscle, liver, kidney, gut, and testis, Thus, the functional interaction between the two proteins in other tissues seems to be of high probability.

However, even though we found that AAC is the main uncoupling protein in several non-adipose tissues such as the heart, skeletal muscle, liver, and kidneys using the mitochondrial patch-clamp technique, we did not measure H^+ current across IMM in every tissue, including cells from the nervous system [7,10]. Moreover, our measurements of the AAC-dependent H^+ flux, using pH dynamics measurements, has only been performed in C2C12 cells.

Thus, to generalize our findings, it will be necessary to perform similar pH measurements in other cell types.

4.4. AAC as potential target against diseases affecting mitochondrial functions

Cell metabolism is closely intertwined with and controlled by mitochondrial function and bioenergetics [17,38]. It is therefore not surprising that most common diseases involve mitochondrial dysfunction. Understanding the mechanisms that control mitochondrial bioenergetics, including how energy is distributed between heat and ATP, will open new therapeutic avenues. Recent results have shown that inhibition of the reverse activity of the ATP synthase preserves matrix ATP levels in cells with mitochondrial dysfunction [2,58]. Moreover, uncouplers have demonstrated effectiveness in combating the oxidative stress encountered in cases of ischemia/reperfusion, diabetes, aging, neurodegenerative diseases, and brain injury [29,32,40,47,48,64]. The use of BAM15 as an inducer of AAC-dependent H^+ transport across the IMM demonstrated for the first time how the dual functions of AAC oversee mitochondrial bioenergetics. AAC and ATP synthase are functionally linked not only for cellular ATP requirements but also for the strict control of the H^+ pool across the IMM.

In conclusion, AAC represents a new target for controlling the distribution of mitochondrial energy between ATP and heat to alter cellular metabolism and could therefore yield promising therapeutic benefits.

CRediT authorship contribution statement

Bernard Ribalet: Writing – original draft, Visualization, Validation, Software, Project administration, Methodology, Investigation, Formal analysis, Data curation, Conceptualization. **Scott John:** Resources, Methodology, Investigation, Formal analysis. **Madeleine G. Milner:** Software, Methodology, Investigation, Funding acquisition, Formal analysis. **Leia Salongo:** Methodology, Investigation, Formal analysis. **Bertholet Ambre Marguerite:** Writing – review & editing, Writing – original draft, Visualization, Validation, Supervision, Software, Resources, Project administration, Methodology, Investigation, Funding acquisition, Formal analysis, Data curation, Conceptualization.

Declaration of Competing Interest

The authors declare the following financial interests/personal relationships which may be considered as potential competing interests: Ambre Bertholet reports financial support was provided by National Institutes of Health. If there are other authors, they declare that they have no known competing financial interests or personal relationships that could have appeared to influence the work reported in this paper.

Acknowledgments

We thank the Bertholet laboratory for helpful discussions. We thank Farha Khan and Natalia Ermolova for preliminary constructions of AAC1. We thank Linsey Stiles from the Metabolism Center at UCLA for valuable experimental advice and training. We thank Ajit Divakaruni for constructive feedback on our manuscript. We would like to thank Professor Paolo Bernardi for his many years of support. A. M. B. is supported by National Institutes of Health grants R35GM143097 and P30 DK063491 as well as the Pew Scholars in Biomedical Sciences. M.G.M is supported by American Heart Association predoctoral grant 25PRE1374054.

Appendix A. Supporting information

Supplementary data associated with this article can be found in the online version at doi:10.1016/j.phrs.2025.107973.

Data availability

Data will be made available on request.

References

[1] M.F. Abad, G. Di Benedetto, P.J. Magalhaes, L. Filippin, T. Pozzan, Mitochondrial pH monitored by a new engineered green fluorescent protein mutant, J Biol Chem 279 (2004) 11521–11529.
[2] R. Acin-Perez, C. Beninca, L. Fernandez Del Rio, C. Shu, S. Baghdasarian, V. Zanette, C. Gerle, C. Jiko, R. Khairallah, S. Khan, et al., Inhibition of ATP synthase reverse activity restores energy homeostasis in mitochondrial pathologies, EMBO J. 42 (2023) e111699.
[3] A. Almeida, S. Moncada, J.P. Bolanos, Nitric oxide switches on glycolysis through the AMP protein kinase and 6-phosphofructo-2-kinase pathway, Nat. Cell Biol. 6 (2004) 45–51.
[4] C.L. Axelrod, W.T. King, G. Davuluri, R.C. Noland, J. Hall, M. Hull, W.S. Dantas, E. R. Zunica, S.J. Alexopoulos, K.L. Hoehn, et al., BAM15-mediated mitochondrial uncoupling protects against obesity and improves glycemic control, EMBO Mol. Med 12 (2020) e12088.
[5] P. Bernardi, C. Gerle, A.P. Halestrap, E.A. Jonas, J. Karch, N. Mnatsakanyan, E. Pavlov, S.S. Sheu, A.A. Soukas, Identity, structure, and function of the mitochondrial permeability transition pore: controversies, consensus, recent advances, and future directions, Cell Death Differ. 30 (2023) 1869–1885.
[6] A.M. Bertholet, The use of the Patch-Clamp technique to study the thermogenic capacity of mitochondria, J. Vis. Exp. (2021).
[7] A.M. Bertholet, E.T. Chouchani, L. Kazak, A. Angelin, A. Fedorenko, J.Z. Long, S. Vidoni, R. Garrity, J. Cho, N. Terada, et al., H(+) transport is an integral function of the mitochondrial ADP/ATP carrier, Nature 571 (2019) 515–520.
[8] A.M. Bertholet, L. Kazak, E.T. Chouchani, M.G. Bogaczynska, I. Paranjpe, G. L. Wainwright, A. Betourne, S. Kajimura, B.M. Spiegelman, Y. Kirichok, Mitochondrial patch clamp of beige adipocytes reveals UCP1-Positive and UCP1-Negative cells both exhibiting futile creatine cycling, Cell Metab. 25 (2017) 811–822, e814.
[9] A.M. Bertholet, Y. Kirichok, The mechanism FA-Dependent H(+) transport by UCP1, Handb. Exp. Pharmacol. 251 (2019) 143–159.
[10] A.M. Bertholet, Y. Kirichok, Mitochondrial H(+) leak and thermogenesis, Annu Rev. Physiol. (2021).
[11] A.M. Bertholet, A.M. Natale, P. Bisignano, J. Suzuki, A. Fedorenko, J. Hamilton, T. Brustovetsky, L. Kazak, R. Garrity, E.T. Chouchani, et al., Mitochondrial uncouplers induce proton leak by activating AAC and UCP1, Nature 606 (2022) 180–187.
[12] J.C. Boffi, J. Knabbe, M. Kaiser, T. Kuner, KCC2-dependent Steady-state intracellular chloride concentration and ph in cortical layer 2/3 neurons of anesthetized and awake mice, Front. Cell Neurosci. 12 (2018) 7.
[13] F. Bouillaud, UCP2, not a physiologically relevant uncoupler but a glucose sparing switch impacting ROS production and glucose sensing, Biochim. Biophys. Acta 1787 (2009) 377–383.
[14] F. Bouillaud, M.C. Alves-Guerra, D. Ricquier, UCPs, at the interface between bioenergetics and metabolism, Biochim. Biophys. Acta 1863 (2016) 2443–2456.
[15] M.J. Bround, D.M. Bers, J.D. Molkentin, A 20/20 view of ANT function in mitochondrial biology and necrotic cell death, J. Mol. Cell Cardiol. (2020).
[16] M. Campanella, N. Parker, C.H. Tan, A.M. Hall, M.R. Duchen, IF(1): setting the pace of the F(1)F(o)-ATP synthase, Trends Biochem. Sci. 34 (2009) 343–350.
[17] N.S. Chandel, Mitochondria, Cold Spring Harb. Perspect. Biol. 13 (2021).
[18] C. Chen, Y. Ko, M. Delannoy, S.J. Ludtke, W. Chiu, P.L. Pedersen, Mitochondrial ATP synthasome: three-dimensional structure by electron microscopy of the ATP synthase in complex formation with carriers for pi and ADP/ATP, J. Biol. Chem. 279 (2004) 31761–31768.
[19] E.S. Childress, S.J. Alexopoulos, K.L. Hoehn, W.L. Santos, Small molecule mitochondrial uncouplers and their therapeutic potential, J. Med. Chem. 61 (2018) 4641–4655.
[20] C. Chinopoulos, V. Adam-Vizi, Mitochondria as ATP consumers in cellular pathology, Biochim. Biophys. Acta 1802 (2010) 221–227.
[21] E.T. Chouchani, L. Kazak, B.M. Spiegelman, New advances in adaptive thermogenesis: UCP1 and beyond, Cell Metab. 29 (2019) 27–37.
[22] S.M. Claypool, Y. Oktay, P. Boontheung, J.A. Loo, C.M. Koehler, Cardiolipin defines the interactome of the major ADP/ATP carrier protein of the mitochondrial inner membrane, J. Cell Biol. 182 (2008) 937–950.
[23] F. De Leonardis, A. Ahmed, A. Vozza, L. Capobianco, C.L. Riley, S.N. Barile, D. Di Molfetta, S. Tiziani, J. DiGiovanni, L. Palmieri, et al., Human mitochondrial uncoupling protein 3 functions as a metabolite transporter, FEBS Lett. 598 (2024) 338–346.
[24] M.R. Depaoli, F. Karsten, C.T. Madreiter-Sokolowski, C. Klec, B. Gottschalk, H. Bischof, E. Eroglu, M. Waldeck-Weiermair, T. Simmen, W.F. Graier, et al., Real-Time imaging of mitochondrial ATP dynamics reveals the metabolic setting of single cells, Cell Rep. 25 (2018) 501–512, e503.
[25] A.S. Divakaruni, M.D. Brand, The regulation and physiology of mitochondrial proton leak, Physiol. (Bethesda) 26 (2011) 192–205.
[26] A.S. Divakaruni, A. Paradyse, D.A. Ferrick, A.N. Murphy, M. Jastroch, Analysis and interpretation of microplate-based oxygen consumption and ph data, Methods Enzym. 547 (2014) 309–354.
[27] A. Fedorenko, P.V. Lishko, Y. Kirichok, Mechanism of fatty-acid-dependent UCP1 uncoupling in brown fat mitochondria, Cell 151 (2012) 400–413.
[28] A. Flierl, S.E. Schriner, S. Hancock, P.E. Coskun, D.C. Wallace, The mitochondrial adenine nucleotide transporters in myogenesis, Free Radic. Biol. Med. 188 (2022) 312–327.
[29] J.G. Geisler, K. Marosi, J. Halpern, M.P. Mattson, DNP, mitochondrial uncoupling, and neuroprotection: a little dab'll do ya, Alzheimers Dement 13 (2017) 582–591.

[30] S. John, G. Calmettes, S. Xu, B. Ribalet, Real-time resolution studies of the regulation of pyruvate-dependent lactate metabolism by hexokinases in single cells, PLoS One 18 (2023) e0286660.
[31] S. John, G. Calmettes, S. Xu, B. Ribalet, Real-time resolution studies of the regulation of lactate production by hexokinases binding to mitochondria in single cells, PLoS One 19 (2024) e0300150.
[32] B.M. Kenwood, J.L. Weaver, A. Bajwa, I.K. Poon, F.L. Byrne, B.A. Murrow, J. A. Calderone, L. Huang, A.S. Divakaruni, J.L. Tomsig, et al., Identification of a novel mitochondrial uncoupler that does not depolarize the plasma membrane, Mol. Metab. 3 (2014) 114–123.
[33] M. Klingenberg, The ADP and ATP transport in mitochondria and its carrier, Biochim. Biophys. Acta 1778 (2008) 1978–2021.
[34] Y.H. Ko, M. Delannoy, J. Hullihen, W. Chiu, P.L. Pedersen, Mitochondrial ATP synthasome. Cristae-enriched membranes and a multiwell detergent screening assay yield dispersed single complexes containing the ATP synthase and carriers for pi and ADP/ATP, J. Biol. Chem. 278 (2003) 12305–12309.
[35] J. Kreiter, T. Tyschuk, E.E. Pohl, Uncoupling protein 3 catalyzes the exchange of C4 metabolites similar to UCP2, Biomolecules 14 (2023).
[36] S.E. Levy, Y.S. Chen, B.H. Graham, D.C. Wallace, Expression and sequence analysis of the mouse adenine nucleotide translocase 1 and 2 genes, Gene 254 (2000) 57–66.
[37] Y.W. Lu, M.G. Acoba, K. Selvaraju, T.C. Huang, R.S. Nirujogi, G. Sathe, A. Pandey, S.M. Claypool, Human adenine nucleotide translocases physically and functionally interact with respirasomes, Mol. Biol. Cell 28 (2017) 1489–1506.
[38] I. Martinez-Reyes, N.S. Chandel, Cancer metabolism: looking forward, Nat. Rev. Cancer 21 (2021) 669–680.
[39] G. Miesenbock, D.A. De Angelis, J.E. Rothman, Visualizing secretion and synaptic transmission with pH-sensitive Green fluorescent proteins, Nature 394 (1998) 192–195.
[40] J. Minners, E.J. van den Bos, D.M. Yellon, H. Schwalb, L.H. Opie, M.N. Sack, Dinitrophenol, cyclosporin A, and trimetazidine modulate preconditioning in the isolated rat heart: support for a mitochondrial role in cardioprotection, Cardiovasc. Res. 47 (2000) 68–73.
[41] J. Mozo, G. Ferry, A. Studeny, C. Pecqueur, M. Rodriguez, J.A. Boutin, F. Bouillaud, Expression of UCP3 in CHO cells does not cause uncoupling, but controls mitochondrial activity in the presence of glucose, Biochem. J. 393 (2006) 431–439.
[42] M.Y. Ng, Z.J. Song, C.H. Tan, M. Bassetto, T. Hagen, Structural investigations on the mitochondrial uncouplers niclosamide and FCCP, FEBS Open Bio 14 (2024) 1057–1071.
[43] D.G. Nicholls, S.L. Budd, Mitochondria and neuronal survival, Physiol. Rev. 80 (2000) 315–360.
[44] O.B. Ogunbona, M.G. Baile, S.M. Claypool, Cardiomyopathy-associated mutation in the ADP/ATP carrier reveals translation-dependent regulation of cytochrome c oxidase activity, Mol. Biol. Cell 29 (2018) 1449–1464.
[45] L. Palmieri, S. Alberio, I. Pisano, T. Lodi, M. Meznaric-Petrusa, J. Zidar, A. Santoro, P. Scarcia, F. Fontanesi, E. Lamantea, et al., Complete loss-of-function of the heart/muscle-specific adenine nucleotide translocator is associated with mitochondrial myopathy and cardiomyopathy, Hum. Mol. Genet. 14 (2005) 3079–3088.
[46] S. Papa, P.L. Martino, G. Capitanio, A. Gaballo, D. De Rasmo, A. Signorile, V. Petruzzella, The oxidative phosphorylation system in mammalian mitochondria, Adv. Exp. Med. Biol. 942 (2012) 3–37.
[47] R.J. Perry, T. Kim, X.M. Zhang, H.Y. Lee, D. Pesta, V.B. Popov, D. Zhang, Y. Rahimi, M.J. Jurczak, G.W. Cline, et al., Reversal of hypertriglyceridemia, fatty liver disease, and insulin resistance by a liver-targeted mitochondrial uncoupler, Cell Metab. 18 (2013) 740–748.
[48] R.J. Perry, D. Zhang, X.M. Zhang, J.L. Boyer, G.I. Shulman, Controlled-release mitochondrial protonophore reverses diabetes and steatohepatitis in rats, Science 347 (2015) 1253–1256.
[49] R. Quintana-Cabrera, C. Quirin, C. Glytsou, M. Corrado, A. Urbani, A. Pellattiero, E. Calvo, J. Vazquez, J.A. Enriquez, C. Gerle, et al., The cristae modulator optic atrophy 1 requires mitochondrial ATP synthase oligomers to safeguard mitochondrial function, Nat. Commun. 9 (2018) 3399.
[50] B. Rieger, T. Arroum, M.T. Borowski, J. Villalta, K.B. Busch, Mitochondrial F(1) F (O) ATP synthase determines the local proton motive force at cristae rims, EMBO Rep. 22 (2021) e52727.
[51] A.J. Rossano, A.K. Chouhan, G.T. Macleod, Genetically encoded pH-indicators reveal activity-dependent cytosolic acidification of drosophila motor nerve termini in vivo, J. Physiol. 591 (2013) 1691–1706.
[52] J. Santo-Domingo, M. Giacomello, D. Poburko, L. Scorrano, N. Demaurex, OPA1 promotes pH flashes that spread between contiguous mitochondria without matrix protein exchange, EMBO J 32 (2013) 1927–1940.
[53] N. Senoo, S. Kandasamy, O.B. Ogunbona, M.G. Baile, Y. Lu, S.M. Claypool, Cardiolipin, conformation, and respiratory complex-dependent oligomerization of the major mitochondrial ADP/ATP carrier in yeast, Sci. Adv. 6 (2020) eabb0780.
[54] D.P. Shah, C.S. Vancuylenburg, E.M. Olzomer, S.Y. Chen, R.J. Grams, M. Beretta, F. L. Byrne, W.L. Santos, K.L. Hoehn, Diverse actions of 15 structurally unrelated mitochondrial uncouplers in cells and mice, Mol. Metab. 99 (2025) 102204.
[55] V.P. Skulachev, A.A. Sharaf, L.S. Yagujzinsky, A.A. Jasaitis, E.A. Liberman, V. P. Topali, The effect of uncouplers on mitochondria, respiratory enzyme complexes and artificial phospholipid membranes, Curr. Mod. Biol. 2 (1968) 98–105.
[56] H. Terada, Uncouplers of oxidative phosphorylation, Environ. Health Perspect. 87 (1990) 213–218.
[57] L. Tommasin, A. Carrer, F.B. Nata, E. Frigo, F. Fogolari, G. Lippe, M. Carraro, P. Bernardi, Adenine nucleotide translocator and ATP synthase cooperate in mediating the mitochondrial permeability transition, J. Physiol. (2025).
[58] G.E. Valdebenito, A.R. Chacko, M.R. Duchen, The mitochondrial ATP synthase as an ATP consumer-a surprising therapeutic target, EMBO J. 42 (2023) e114141.
[59] V. Venkatachalam, A.E. Cohen, Imaging GFP-based reporters in neurons with multiwavelength optogenetic control, Biophys. J. 107 (2014) 1554–1563.
[60] A.D. Vinogradov, New perspective on the reversibility of ATP synthesis and hydrolysis by FoxF1-ATP synthase (Hydrolase), Biochemistry (Mosc) 84 (2019) 1247–1255.
[61] A. Vozza, G. Parisi, F. De Leonardis, F.M. Lasorsa, A. Castegna, D. Amorese, R. Marmo, V.M. Calcagnile, L. Palmieri, D. Ricquier, et al., UCP2 transports C4 metabolites out of mitochondria, regulating glucose and glutamine oxidation, Proc. Natl. Acad. Sci. USA 111 (2014) 960–965.
[62] D. White, 3rd, Q. Yang, Genetically encoded ATP biosensors for direct monitoring of cellular ATP dynamics, Cells 11 (2022).
[63] H. Zhang, N.N. Alder, W. Wang, H. Szeto, D.J. Marcinek, P.S. Rabinovitch, Reduction of elevated proton leak rejuvenates mitochondria in the aged cardiomyocyte, eLife 9 (2020).
[64] R. Zhong, D.L.A. Dionela, N.H. Kim, E.N. Harris, J.G. Geisler, L. Wei-LaPierre, Micro-Doses of DNP preserve motor and muscle function with a period of functional recovery in amyotrophic lateral sclerosis mice, Ann. Neurol. 97 (2025) 542–557.
[65] L.D. Zorova, V.A. Popkov, E.Y. Plotnikov, D.N. Silachev, I.B. Pevzner, S. S. Jankauskas, V.A. Babenko, S.D. Zorov, A.V. Balakireva, M. Juhaszova, et al., Mitochondrial membrane potential, Anal. Biochem. 552 (2018) 50–59.